Astronomy & Astrophysics manuscript no. DGS˙photometry˙submission˙revised
September 6, 2013

Revealing the cold dust in low-metallicity environments: I - Photometry analysis of the Dwarf Galaxy Survey with *Herschel*

A. Rémy-Ruyer[1], S.C. Madden[1], F. Galliano[1], S. Hony[1], M. Sauvage[1], G. J. Bendo[2], H. Roussel[3], M. Pohlen[4], M. W. L. Smith[4], M. Galametz[5], D. Cormier[1], V. Lebouteiller[1], R. Wu[1], M. Baes[6], M. J. Barlow[7], M. Boquien[8], A. Boselli[8], L. Ciesla[9], I. De Looze[6], O. Ł. Karczewski[7], P. Panuzzo[10], L. Spinoglio[11], M. Vaccari[12], C.D. Wilson[13], and the *Herschel*-SAG2 consortium.

[1] Laboratoire AIM, CEA, Université Paris Sud XI, IRFU/Service d'Astrophysique, Bat. 709, 91191 Gif-sur-Yvette, France, e-mail: aurelie.remy@cea.fr

[2] UK ALMA Regional Centre Node, Jodrell Bank Centre for Astrophysics, School of Physics & Astronomy, University of Manchester, Oxford Road, Manchester M13 9PL, UK

[3] Institut d'Astrophysique de Paris, UMR7095 CNRS, Université Pierre & Marie Curie, 98 bis Boulevard Arago, 75014 Paris, France

[4] School of Physics & Astronomy, Cardiff University, The Parade, Cardiff, CF24 3AA, UK

[5] Institute of Astronomy, University of Cambridge, Madingley Road, Cambridge CB3 0HA, UK

[6] Sterrenkundig Observatorium, Universiteit Gent, Krijgslaan 281 S9, B-9000 Gent, Belgium

[7] Department of Physics and Astronomy, University College London, Gower St, London WC1E 6BT, UK

[8] Laboratoire dAstrophysique de Marseille - LAM, Université dAix-Marseille & CNRS, UMR7326, 38 rue F. Joliot-Curie, 13388 Marseille Cedex 13, France

[9] Department of Physics, University of Crete, GR-71003, Heraklion, Greece

[10] GEPI, Observatoire de Paris, CNRS, Univ. Paris Diderot, Place Jules Janssen 92190 Meudon, France

[11] Instituto di Astrofisica e Planetologia Spaziali, INAF-IAPS, Via Fosso del Cavaliere 100, I-00133 Roma, Italy

[12] Physics Department, University of the Western Cape, Private Bag X17, 7535, Bellville, Cape Town, South Africa

[13] Department of Physics & Astronomy, McMaster University, Hamilton Ontario L8S 4M1 Canada

Received date/Accepted date

ABSTRACT

Context. We present new photometric data from our *Herschel* Guaranteed Time Key Programme, the Dwarf Galaxy Survey (DGS), dedicated to the observation of the gas and dust in low-metallicity environments. A total of 48 dwarf galaxies were observed with the PACS and SPIRE instruments onboard the *Herschel* Space Observatory at 70, 100, 160, 250, 350, and 500 μm.

Aims. The goal of this paper is to provide reliable far infrared (FIR) photometry for the DGS sample and to analyse the FIR/submillimetre (submm) behaviour of the DGS galaxies. We focus on a systematic comparison of the derived FIR properties (FIR luminosity, L_{FIR}, dust mass, M_{dust}, dust temperature, T, emissivity index, β) with more metal-rich galaxies and investigate the detection of a potential submm excess.

Methods. The data reduction method is adapted for each galaxy in order to derive the most reliable photometry from the final maps. The derived PACS flux densities are compared with the *Spitzer* MIPS 70 and 160 μm bands. We use colour-colour diagrams to analyse the FIR/submm behaviour of the DGS galaxies and modified blackbody fitting procedures to determine their dust properties. To study the variation in these dust properties with metallicity, we also include galaxies from the *Herschel* KINGFISH sample, which contains more metal-rich environments, totalling 109 galaxies.

Results. The location of the DGS galaxies on *Herschel* colour-colour diagrams highlights the differences in dust grain properties and/or global environments of low-metallicity dwarf galaxies. The dust in DGS galaxies is generally warmer than in KINGFISH galaxies ($T_{DGS} \sim 32$ K and $T_{KINGFISH} \sim 23$ K). The emissivity index, β, is ~ 1.7 in the DGS, however metallicity does not make a strong effect on β. The proportion of dust mass relative to stellar mass is lower in low-metallicity galaxies: $M_{dust}/M_{star} \sim 0.02\%$ for the DGS versus 0.1% for KINGFISH. However, per unit dust mass, dwarf galaxies emit about six times more in the FIR/submm than higher metallicity galaxies. Out of the 22 DGS galaxies detected at 500 μm, about 41% present an excess in the submm beyond the explanation of our dust SED model, and this excess can go up to 150% above the prediction from the model. The excess mainly appears in lower metallicity galaxies (12+log(O/H) $\lesssim 8.3$), and the strongest excesses are detected in the most metal-poor galaxies. However, we also stress the need for observations longwards of the *Herschel* wavelengths to detect any submm excess appearing beyond 500 μm.

Key words. galaxies:ISM - galaxies:dwarf - galaxies:photometry - infrared:galaxies - infrared:ISM - ISM:dust, extinction

1. Introduction

The continuous interplay between stars and the interstellar medium (ISM) is one of the major drivers of galaxy evolution. The ISM is primarily composed of gas and dust, and it plays a key role in this evolution, as the repository of stellar ejecta and the site of stellar birth. It thus contains the imprint of the astrophysical processes occurring in a galaxy. Interstellar dust is present in most phases of the ISM, from warm ionized regions around young stars to the cores of dense molecular clouds. Because dust is mainly formed from the available metals in the ISM, the dust content traces its internal evolution through metal enrichment. Dust thus influences the subsequent star formation and has a significant impact on the total spectral energy distribution (SED) of a galaxy: the absorbed stellar light by dust in the ultraviolet (UV) and visible wavelengths is re-emitted in the infrared (IR) domain by the dust grains. In our Galaxy, dust reprocesses about 30% of the stellar power, and it can grow to as large as $\sim$ 99% in a starburst galaxy. Studying the IR emission of galaxies thus provides valuable information on the dust properties of the galaxies and on their overall star formation activity.

Our Galaxy, as well as other well studied local Universe galaxies, provide various observational benchmarks to calibrate the physical dust properties around solar metallicity. However, for galaxies of the high-redshift Universe, dust properties are still poorly known, due to observational constraints and to the unsure variations in dust properties as the metallicity decreases. Because of their low metal abundance and active star formation, dwarf galaxies of the local Universe are ideal laboratories for studying star formation and its feedback on the ISM in conditions that may be representative of different stages in early Universe environments.

From *IRAS* to *Spitzer*, many studies have been dedicated to dwarf galaxies over the past decades, and have uncovered peculiar ISM properties compared to their metal-rich counterparts. Among these, are the following:

Overall warmer dust: the SEDs in some low-metallicity star-forming dwarf galaxies often peak at shorter wavelengths, sometimes well below 100 μm, whereas for more metal-rich galaxies, the peak of the SED is around 100 - 200 μm (Galliano et al. 2003, 2005; Walter et al. 2007; Engelbracht et al. 2008; Galametz et al. 2009). This is a consequence of the harder interstellar radiation field (ISRF) interacting with the porous ISM of dwarf galaxies (e.g. Madden et al. 2006).

Weak mid infrared (MIR) aromatic features: the polycyclic aromatic hydrocarbons (PAHs) are often barely detected, if at all, in these galaxies (e.g. Sauvage et al. 1990; Madden 2000; Boselli et al. 2004; Engelbracht et al. 2005). The combination of young star clusters and metal-poor ISM creates a harder galaxy-wide radiation field compared to that of our Galaxy. The paucity of dust allows the harder UV photons to travel deeper into the ISM and destroy PAH molecules by photoevaporation or photodissociation (Galliano et al. 2003, 2005; Madden et al. 2006). The dearth of PAH features in dwarf galaxies has also been explained by the destruction of the molecules by supernovae (SN) shocks (O'Halloran et al. 2006) or by a delayed carbon injection in the ISM by asymptotic giant branch (AGB) stars (Galliano et al. 2008).

The submillimetre (submm) excess: an excess emission, unaccountable by usual SED models, is appearing in the FIR to submm/millimetre (mm) domain for some dwarf galaxies (Galliano et al. 2003, 2005; Galametz et al. 2009; Bot et al. 2010; Grossi et al. 2010). An excess emission has also been observed in our Galaxy with COBE (Reach et al. 1995) but with an intensity less pronounced compared to that found in low-metallicity systems. Dumke et al. (2004); Bendo et al. (2006); Zhu et al. (2009) found a submm excess in some low-metallicity spiral galaxies as well. The discovery of this excess renders even more uncertain the determination of a quantity as fundamental as the dust mass.

The faint CO emission: CO is difficult to observe in dwarf galaxies (i.e. Leroy et al. 2009; Schruba et al. 2012), and the determination of the molecular gas reservoir at low metallicities through the usual CO-to-H_2 conversion factor is still very uncertain. The dependence of the CO-to-H_2 conversion factor on metallicity has been studied extensively (Wilson 1995; Boselli et al. 2002; Leroy et al. 2011; Schruba et al. 2012) but have been limited to metallicities greater than $\sim$ 1/5 $Z_\odot$[1] due to the difficulty of detecting CO at lower metallicities. This renders accurate determinations of gas-to-dust mass ratios (G/D) very difficult, as H_2 may account for a significant fraction of the total (atomic HI and molecular H_2) gas mass. We now believe that the structure of molecular clouds in dwarf galaxies is very different from that of metal-rich systems, and that CO does not trace the full molecular gas reservoir. A potentially large reservoir of CO-dark molecular gas could exist in low-metallicity galaxies, traceable by the FIR cooling line [CII] (Poglitsch et al. 1995; Israel et al. 1996; Madden et al. 1997, 2012), or by neutral carbon [CI] (Papadopoulos et al. 2004; Wilson 2005).

The wavelength ranges and sensitivities covered by *Spitzer*, *Infrared Space Observatory* (*ISO*) and *IRAS* do not sample the cold dust component of the dust SED beyond 160 μm. Some ground-based telescopes such as *JCMT*, *APEX*, *SEST*, *IRAM* could detect the cold dust beyond 160 μm, but because of sensitivity limitations, accurate measures of the photometry could only be obtained for the brightest and highest metallicity dwarf galaxies. The *Herschel* Space Observatory (Pilbratt et al. 2010), launched in 2009, is helping to fill this gap and complete our view of dust in galaxies by constraining the cold dust contribution. *Herschel* covers a wide range of wavelengths in the FIR and submm, with unprecedented resolution: its 3.5 m diameter mirror is the largest ever launched in space so far for this wavelength range. *Herschel* carries three instruments among which are the Photodetector Array Camera and Spectrometer (PACS - Poglitsch et al. 2010) and the Spectral and Photometric Imaging REceiver (SPIRE - Griffin et al. 2010), both imaging photometres and medium resolution spectrometres. The PACS and SPIRE photometres in combination cover a 70 to 500 μm range, and the spectrometres together cover 55 to 670 μm.

We focus here on local dwarf galaxies by presenting new results of the *Herschel* Guaranteed Time Key Progam, the Dwarf Galaxy Survey (DGS - P.I. Madden ; Madden et al. 2013). Dwarf galaxies are studied here in a systematic way, enabling us to derive general properties that are representative of these systems. We will focus our study on overall dust properties and look at the submm excess. We present the observed sample and the data reduction processes in Section 2. We then present the flux extraction method and the flux catalogues for the whole sample in Section 3. Section 4 is dedicated to the comparison of the dwarf galaxies with more metal-rich environments, first qualitatively with colour-colour diagrams, and then quantitatively with modified blackbody fits. We also inspect a sub-sample of galaxies presenting a submm excess. Throughout this last Section we compare our results with those from another *Herschel* sample, KINGFISH (Kennicutt et al. 2011), which is probing predomi-

[1] Throughout, we assume $(O/H)_\odot = 4.90 \times 10^4$, i.e., $12+\log(O/H)_\odot = 8.69$ (Asplund et al. 2009)

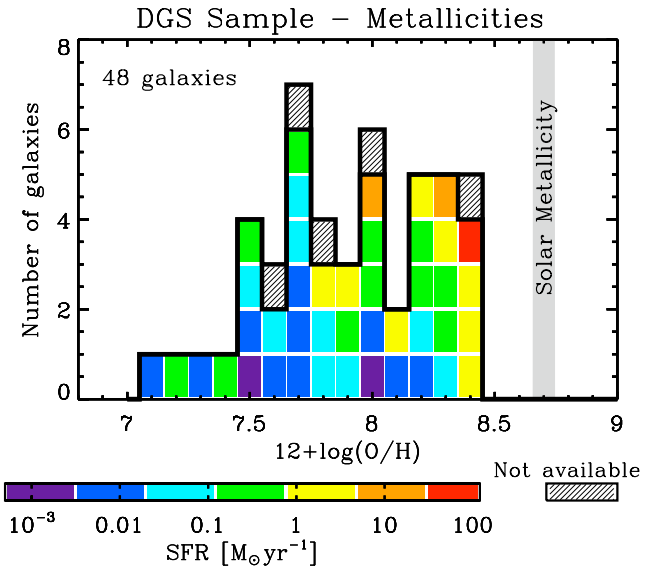

Fig. 1. Metallicity distribution of the DGS sample from 12+log(O/H) = 7.14 to 8.43. Solar metallicity is indicated here as a guide to the eye. The pre-*Herschel* star formation rate (*SFR*) distribution is also indicated by the colour code. They have been converted from L_{TIR}(*Spitzer*) with the Kennicutt (1998) law, and are given in Madden et al. (2013). When no IR data was available, *Hα* or *Hβ* emission lines were used and converted to *SFR* (Kennicutt 1998). The dashed cells indicate that none of these data were available for the galaxy. The most actively star-forming galaxy (in red) corresponds to the starburst luminous infrared galaxy (LIRG) Haro 11.

nantely more metal-rich environments, in order to study the various overall effects of metallicity on the derived dust properties.

2. Observations and Data reduction

2.1. The Dwarf Galaxy Survey with Herschel

2.1.1. Sample

The DGS aims at studying the gas and dust properties in low-metallicity ISMs with the *Herschel* Space Observatory. It is a photometric and spectroscopic survey of 50 dwarf galaxies at FIR and submm wavelengths (Madden et al. 2013). For a more detailed description of the general goals of the survey and the source selection process, see the Dwarf Galaxy Survey Overview by Madden et al. (2013). Here, we focus on the 48 targets for which complete photometry was obtained. The names, positions, distances and metallicities of the DGS galaxies are listed in Table 1 (from Madden et al. 2013).

These targets span a wide range in metallicity from 12+log(O/H) = 7.14 to 8.43, including I Zw 18 with Z ∼ 1/40 $Z_\odot$ (Lequeux et al. 1979; Izotov et al. 1999) which is one of the most metal-poor galaxies in the local Universe known to date (see Figure 1 for the metallicity distribution of the DGS targets).

2.1.2. Observations

The Dwarf Galaxy Survey was granted ∼ 230 hours of observations, part of which were used to observe the sample with the two *Herschel* imaging photometres: all of them (48) with PACS at 70, 100 and 160 μm and 41 with SPIRE at 250, 350 and 500 μm. Seven sources were not observed with SPIRE because they were predicted to be too faint for SPIRE. The full width at half maximum (FWHM) of the beam in each band is 5.6, 6.8, 11.4[2], 18.2, 24.9, 36.3″[3] at 70, 100, 160, 250, 350 and 500 μm respectively. Most of the sources have also been observed by the PACS spectrometre in order to complement the photometry (e.g. Cormier et al. 2011, 2012; Lebouteiller et al. 2012; Madden et al. 2013, Cormier et al. 2013, in prep.).

For all of our galaxies, the PACS photometry observations have been done in the PACS scan-map mode at a medium scan speed (20″/s). The SPIRE observations have been made using the SPIRE large and small scan-map modes, depending on the source sizes, at the nominal scan speed (30″/s).

Substantial ancillary data are available over a large wavelength range, from UV to radio wavelengths. A summary of all the available ancillary data for these galaxies is presented in Madden et al. (2013).

2.2. Data reduction process

In this section we describe the data reduction process followed to produce the final *Herschel* maps.

2.2.1. PACS data reduction

For the PACS data reduction we use the *Herschel* Interactive Processing Environment (HIPE, Ott 2010), with version 7 of the photometric calibration[4], and a modified version of the available pipeline which we describe here.

The pipeline begins with the Level 0 Products, at a purely instrumental level. All the auxiliary data (such as "housekeeping" parameters, pointings, etc) is stored as Products. Level 0 also contains the Calibration Tree, needed for flux conversion. Then we perform the usual steps such as flagging the "bad" saturated pixels, converting the signal into Jy·pix^{-1} and applying flatfield correction. We systematically mask the column 0 of all the matrices (the PACS array is composed of groups of 16×16 bolometres) to avoid electrical crosstalk issues. We perform second level deglitching to remove all the glitches, which represent on average ∼ 0.3% of the data.

After performing all of the above steps we reach the Level 1 stage of data reduction. Note that we still have the bolometre drifts (the so-called "1/*f*" noise) at this stage of the data reduction. This low-frequency noise is originating from two sources: thermal noise, strongly correlated between the bolometres, and uncorrelated non-thermal noise. The method employed to remove the drifts will greatly affect the final reconstructed map (also called Level 2 data). We thus analyse three different map making methods in order to systematically compare the maps and extracted flux densities, to determine if there is an optimized method for each galaxy. The first two map making methods are provided in HIPE: the PhotProject and the MADMap method. The last method is the Scanamorphos method (Roussel 2012).

The first technique we use for the final reconstruction of the map is PhotProject. We first remove the 1/*f* noise (correspond-

[2] The PACS Observers' Manual is available at http://herschel.esac.esa.int/ Docs/PACS/pdf/pacs_om.pdf.

[3] The SPIRE Observers' Manual is available at http://herschel.esac.esa.int/Docs/SPIRE/pdf/spire_om.pdf.

[4] The version 7 cited here corresponds to the value of the calFileVersion metadata of the Responsitivity Calibration Product in HIPE.

Table 1. Characteristics of the sample.

Source	RA (J2000)	DEC (J2000)	Distance (Mpc)	Ref	12 + log(O/H)	Ref
Haro 11	00h36m52.7s	-33d33m17.0s	92.1	1	8.36 ± 0.01	1
Haro 2	10h32m32.0s	+54d24m02.0s	21.7	2	8.23 ± 0.03	2
Haro 3	10h45m22.4s	+55d57m37.0s	19.3	3	8.28 ± 0.01	3
He 2-10	08h36m15.1s	-26d24m34.0s	8.7	21	8.43 ± 0.01	4
HS 0017+1055	00h20m21.4s	+11d12m21.0s	79.1	3	7.63 ± 0.10	5
HS 0052+2536	00h54m56.4s	+25d53m08.0s	191.0	3	8.04 ± 0.10[a]	5
HS 0822+3542	08h25m55.5s	+35d32m32.0s	11.0	4	7.32 ± 0. 03	6
HS 1222+3741	12h24m36.7s	+37d24m37.0s	181.7	3	7.79 ± 0.01	7
HS 1236+3937	12h39m20.2s	+39d21m05.0s	86.3	3	7.72 ± 0.10	8
HS 1304+3529	13h06m24.2s	+35d13m43.0s	78.7	3	7.93 ± 0.10	8
HS 1319+3224	13h21m19.7s	+32d08m25.0s	86.3	3	7.81 ± 0.10	8
HS 1330+3651	13h33m08.3s	+36d36m33.0s	79.7	3	7.98 ± 0.10	8
HS 1442+4250	14h44m12.8s	+42d37m44.0s	14.4	3	7.60 ± 0.01	9
HS 2352+2733	23h54m56.7s	+27d49m59.0s	116.7	3	8.40 ± 0.10	5
I Zw 18	09h34m02.0s	+55d14m28.0s	18.2	5	7.14 ± 0.01	10
II Zw 40	05h55m42.6s	+03d23m32.0s	12.1	20	8.23 ± 0.01	12
IC 10	00h20m17.3s	+59d18m14.0s	0.7	6	8.17 ± 0.03	11
Mrk 1089	05h01m37.7s	-04d15m28.0s	56.6	3	8.10 ± 0.08[a]	13
Mrk 1450	11h38m35.7s	+57d52m27.0s	19.8	3	7.84 ± 0.01	14
Mrk 153	10h49m05.0s	+52d20m08.0s	40.3	3	7.86 ± 0.04	15
Mrk 209	12h26m15.9s	+48d29m37.0s	5.8	7	7.74 ± 0.01	16
Mrk 930	23h31m58.3s	+28h56m50.0s	77.8	3	8.03 ± 0.01	17
NGC 1140	02h54m33.6s	-10d01m40.0s	20.0	8	8.38 ± 0.01	3
NGC 1569	04h30m49.0s	+64d50m53.0s	3.1	9	8.02 ± 0.02	18
NGC 1705	04h54m13.5s	-53d21m40.0s	5.1	10	8.27 ± 0.11	19
NGC 2366	07h28m54.6s	+69d12m57.0s	3.2	11	7.70 ± 0.01	20
NGC 4214	12h15m39.2s	+36d19m37.0s	2.9	12	8.26 ± 0.01	4
NGC 4449	12h28m11.1s	+44d05m37.0s	4.2	13	8.20 ± 0.11	21
NGC 4861	12h59m02.3s	+34d51m34.0s	7.5	14	7.89 ± 0.01	16
NGC 5253	13h39m55.9s	-31d38m24.0s	4.0	12	8.25 ± 0.02	4
NGC 625	01h35m04.6s	-41d26m10.0s	3.9	15	8.22 ± 0.02	22
NGC 6822	19h44m57.7s	-14d48m12.0s	0.5	16	7.96 ± 0.01	23
Pox 186	13h25m48.6s	-11d36m38.0s	18.3	3	7.70 ± 0.01	24
SBS 0335-052	03h37m44.0s	-05d02m40.0s	56.0	3	7.25 ± 0.01	17
SBS 1159+545	12h02m02.4s	+54d15m50.0s	57.0	3	7.44 ± 0.01	14
SBS 1211+540	12h14m02.5s	+53d45m17.0s	19.3	3	7.58 ± 0.01	14
SBS 1249+493	12h51m52.5s	+49d03m28.0s	110.8	3	7.68 ± 0.02	25
SBS 1415+437	14h17m01.4s	+43d30m05.0s	13.6	17	7.55 ± 0.01	26
SBS 1533+574	15h34m13.8s	+57d17m06.0s	54.2	3	8.05 ± 0.01	16
Tol 0618-402	06h20m02.5s	-40d18m09.0s	150.8	3	8.09 ± 0.01	27
Tol 1214-277	12h17m17.1s	-28d02m33.0s	120.5	3	7.52 ± 0.01	4
UGC 4483	08h37m03.0s	+69d46m31.0s	3.2	11	7.46 ± 0.02	28
UGCA 20	01h43m14.7s	+19d58m32.0s	11.0	18	7.50 ± 0.02	29
UM 133	01h44m41.3s	+04d53m26.0s	22.7	3	7.82 ± 0.01	4
UM 311	01h15m34.4s	-00d51m46.0s	23.5	3	8.36 ± 0.01[a]	17
UM 448	11h42m12.4s	+00d20m03.0s	87.8	3	8.32 ± 0.01	17
UM 461	11h51m33.3s	-02d22m22.0s	13.2	3	7.73 ± 0.01	15
VII Zw 403	11h27m59.9s	+78d59m39.0s	4.5	19	7.66 ± 0.01	16

References for positions: The positions have been taken from the Nasa/Ipac Extragalactic Database (NED).

References for distances: (1) Bergvall et al. (2006) ; (2) Kennicutt et al. (2003) ; (3) this work, calculated from the redshifts available in NED, the Hubble flow model from Mould et al. (2000) and assuming H_0 = 70 km.s^{-1}.Mpc^{-1} ; (4) Pustilnik et al. (2003) ; (5) Aloisi et al. (2007) ; (6) Kim et al. (2009) ; (7) Schulte-Ladbeck et al. (2001) ; (8) Moll et al. (2007) ; (9) Grocholski et al. (2012) ; (10) Tosi et al. (2001) ; (11) Karachentsev et al. (2002) ; (12) Karachentsev et al. (2004) ; (13) Karachentsev et al. (2003) ; (14) de Vaucouleurs et al. (1991) ; (15) Cannon et al. (2003) ; (16) Gieren et al. (2006) ; (17) Aloisi et al. (2005) ; (18) Sharina et al. (1996) ; (19) Lynds et al. (1998) ; (20) Bordalo et al. (2009) ; (21) Tully (1988)

References for metallicities: (1) Guseva et al. (2012) ; (2) Kong et al. (2002) ; (3) Izotov et al. (2004) ; (4) Kobulnicky et al. (1999) ; (5) Ugryumov et al. (2003) ; (6) Pustilnik et al. (2003) ; (7) Izotov et al. (2007) ; (8) Popescu & Hopp (2000) ; (9) Guseva et al. (2003a) ; (10) Izotov et al. (1999) ; (11) Magrini & Gonçalves (2009) ; (12) Guseva et al. (2000) ; (13) López-Sánchez et al. (2004) ; (14) Izotov et al. (1994) ; (15) Izotov et al. (2006) ; (16) Izotov et al. (1997) ; (17) Izotov & Thuan (1998) ; (18) Kobulnicky & Skillman (1997) ; (19) Lee & Skillman (2004) ; (20) Saviane et al. (2008) ; (21) McCall et al. (1985) ; (22) Skillman et al. (2003) ; (23) Lee et al. (2006) ; (24) Guseva et al. (2007) ; (25) Thuan et al. (1995) ; (26) Guseva et al. (2003b) ; (27) Masegosa et al. (1994) ; (28) van Zee & Haynes (2006) ; (29) van Zee et al. (1996)

[a]: These objects are galaxies within compact groups of galaxies or are parts of other galaxies. The metallicity quoted here is the mean value for the group of objects. For Mrk1089, the group is composed of regions A-C, B, E, F1, F2, H from López-Sánchez et al. (2004). For UM311, the group is composed of regions 1-2-3 of Moles et al. (1994) plus NGC450 and UGC807. For HS0052+2536 the group is composed of HS0052+2536 and HS0052+2537. For all of the objects, the "group" corresponds to the objects included in the aperture used for the photometry (see Section 3.1.1). For the metallicity of the object only, see Madden et al. (2013).

ing to data with low spatial frequencies or large scale structures in the map) using a high-pass filter. We then use PhotProject to reproject the data on the sky. The high-pass filtering step is optimum for compact sources but can lead to suppression of extended features (corresponding to low spatial frequencies) in extended sources.

MADmap (Microwave Anisotropy Dataset mapper) produces maximum likelihood maps from the time ordered data (Cantalupo et al. 2010). The main assumption here is that the noise is uncorrelated from pixel to pixel. However, one component of the $1/f$ noise is strongly correlated from pixel to pixel, as it is due to the thermal drift of the bolometres, and thus not treated by MADmap. Nevertheless, MADmap is more efficient than PhotProject in reconstructing the extended structures within a map.

Scanamorphos is another technique specially developed to process scan observations (Roussel 2012). The particularity of Scanamorphos, compared to MADmap, is that no particular noise model is assumed to deal with the low-frequency noise (the $1/f$ noise). Indeed Scanamorphos takes advantage of the redundancy in the observations, i.e., of the fact that a portion of the sky is observed more than once and by more than one bolometre. The two noise sources contributing to the low-frequency noise are inferred from the redundancy of the data and removed (Roussel 2012). The maps are made using the default parameters. We add the minimap option when reducing data with a field size of the order of 8.4 arcmin. For consistency in the following flux computation, we produce maps with the same pixel sizes for all of the methods: 2, 2 and 4″ for 70, 100 and 160 μm respectively.

2.2.2. PACS data reduction: choosing between PhotProject, MADmap and Scanamorphos

To determine the best mapmaking method for each galaxy (summarized in Table 2), we compute the flux densities (see Section 3.1.1 for PACS flux extraction) for the three bands for the three methods for each galaxy and compare the photometry for the three different methods. For consistency, we use the same apertures for the three different types of maps.

As mentioned above, the PhotProject method is optimized for compact sources. Indeed, the filtering step partly removes large scale structures in the map. It is not adapted for extended sources as this filtering step can sometimes also remove the large scale structures of our sources such as diffuse extended emission (Figure 2), also noted by Aniano et al. (2012) for two extended KINGFISH galaxies. Moreover the source is automatically masked before the high-pass filtering step, and this mask may be too small for extended sources with peculiar morphology, leading to suppression of extended features during the filtering step. Therefore, we decided to take as final, the maps produced by PhotProject for compact sources only.

Some galaxies are not detected in one or several bands. When deriving upper limits on the flux densities for these galaxies, the three methods give very different results. As the "non-detection" criterion is directly linked to the background determination through its contribution to the total flux density and the corresponding uncertainty, we need to choose the method that gives the most reliable background structure. MADmap and Scanamorphos do not have any constraints on the background values, whereas PhotProject is constrained to an average statistically-null background. Because Scanamorphos does not make assumptions on the background, sometimes positive residual noise structures can remain in the maps. MADmap presents features, such as a curved background for some maps, due to a too-simple treatment of missing data. Again, the PhotProject maps here are used because they are the most constrained as far as the background is concerned. Moreover, when the galaxy is not detected at 160 μm it is usually a compact point source at the other PACS wavelengths. So this choice is consistent with the previous choice for compact sources.

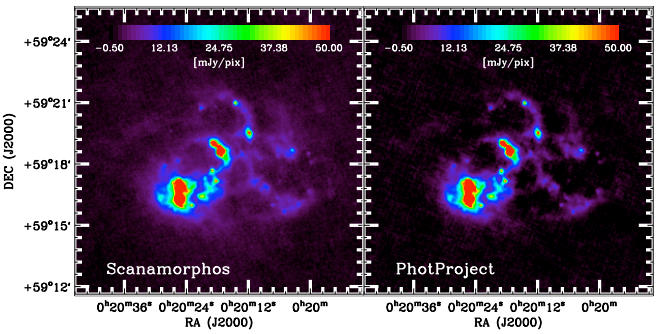

Fig. 2. Scanamorphos (*left*) and PhotProject (*right*) images of IC 10 at 70 μm to illustrate how PhotProject tends to clip out the extended features. The colours and spatial scales are the same on both images. Here the diffuse extended emission is best visible on the Scanamorphos map. The comparison of the total flux densities coming from the 2 methods confirms that PhotProject misses the extended emission: in this case, F_{70}(Scanamorphos)/F_{70}(PhotProject) = 1.5.

For more extended sources, we only consider MADmap and Scanamorphos. As mentioned before, MADmap maps sometimes present a curved background: the source in the map centre is surrounded by lower background levels than those used in the background aperture for the photometry. This therefore results in a high background leading to an underestimation of the source flux density. Moreover this is not consistent with the assumption of a flat background made for the photometry (see Section 3.1.1). To avoid this problem, we decide to use the Scanamorphos maps for the extended sources.

2.2.3. SPIRE data reduction

Following the same method as in Ciesla et al. (2012) for the Herschel Reference Survey, or in Auld et al. (2013) for the HErschel VIrgo Cluster Survey, the SPIRE maps are processed through HIPE[5] using a modified version of the available SPIRE pipeline. The steps from the Level 0 to Level 1 are basically the same as in the official version provided by the SPIRE Instrument Control Centre (ICC). The pipeline starts with a first deglitching step, then a time response correction is applied to match the detector timelines to the astronomical pointing timelines. A second deglitching step is then performed as it improves the removal of residual glitches. After, an additional time response correction, the flux calibration step is performed, where non-linearity corrections are taken into account. An additional correction is applied to the bolometre timelines to account for the fact that there is a delay in the response of the bolometres to the incoming signal. The temperature drifts of the bolometres are then removed. For this step, the pipeline temperature drift removal is not run, instead a custom temperature drift correction (BriGAdE, Smith et al. in prep) is applied to the whole observation timeline (rather than an individual scan-leg). Finally, the Naive mapper is used

[5] The version 5 of HIPE was used for producing the SPIRE maps.

to construct the final map with pixel sizes of 6, 8, 12″ for the 250, 350, 500 μm band respectively. For galaxies with heavy cirrus contamination an additional destriping step is performed. A complete description of the data processing step will be given in Smith et al. in prep.

3. Photometry measurements for the DGS sample

In this section, we describe how we obtain the different PACS and SPIRE flux densities, together with their uncertainties, for the DGS sample (Tables 2 and 3, Sections 3.1 and 3.2). The PACS flux densities are then compared with the existing MIPS flux densities (Section 3.3).

3.1. PACS photometry

3.1.1. Extracting the fluxes

For PACS measurements, we perform aperture photometry, placing an aperture on the source and a background region to estimate the sky level. Using the version 7 of the PACS photometric calibration available in HIPE, the point spread functions (PSFs) have been measured out to 1000″. Most of our maps are smaller than this, which means, in principle, that some contribution from the PSF of the source can basically be found everywhere on the map, and, any emission from the source falling in the background region must be taken into account when estimating the total source flux density.

Taking into account this aperture correction, aperture photometry is performed, using circular apertures of 1.5 times the optical radius whenever possible. For cases where it is not, we adjust our apertures to be sure to encompass all the FIR emission of the galaxy (Table 2). There are three special cases. For HS0052+2536 the chosen aperture also encompasses the neighbouring very faint galaxy HS0052+2537. Mrk1089 is a galaxy within a compact group of galaxies and UM311 is part of another galaxy and the chosen apertures encompass the whole group of objects. For these galaxies, the spatial resolution of the SPIRE bands makes it very difficult, if not impossible, to separate them from the other objects in their respective groups. For these few cases, the entire group is considered and is noted in Tables 1, 2 and 3. The background region is a circular annulus around the source. In most cases, the inner radius of the background region is the same as that of the source aperture and the outer radius is about two times the source aperture radius.

The maps are assumed to consist of the sum of a constant, flat background plus the contribution from the source. Flux densities are measured in the aperture (f_{ap}) and in the background annulus (f_{bg}) by summing the pixels in both regions. The contribution to the measured flux densities (f_{ap} and f_{bg}) from the total flux density of the galaxy (f_{tot}) and from the background (b) is determined for each aperture using the encircled energy fraction (*eef*) tables. These tables, given by HIPE, are measurements of the fraction of the total flux density contained in a given aperture on the PSFs (inverse of the aperture correction). This gives us a simple linear system of two equations with two unknowns: the total flux density from the galaxy (f_{tot}) and the background level (b) :

$$\begin{cases} f_{ap} &= f_{tot} \cdot eef_{r_0} + N_{ap} \cdot b \\ f_{bg} &= f_{tot} \cdot (eef_{r_2} - eef_{r_1}) + N_{bg} \cdot b \end{cases} \quad (1)$$

where r_0, r_1, r_2 are the source aperture radius and the background annulus radii respectively, and eef_{r_0}, eef_{r_1} and eef_{r_2} are the encircled energy fractions at radii r_0, r_1, r_2. N_{ap} (resp. N_{bg}) is the number of pixels in the source (resp. background) aperture. Inverting this system gives us the values for f_{tot} and b.

If one considers that there is no contribution from the source outside the source aperture, i.e. setting eef_{r_0}=1 and eef_{r_1}=eef_{r_2}=0, the flux density will be underestimated, as some contribution from the source will have been removed during the background subtraction. This underestimation depends on the source aperture size r_0 and can be important for small apertures. The error made on the flux density becomes greater than the calibration error, which is the dominant source of uncertainty ($\sim$ 5%, see Section 3.1.2), when $r_0 \lesssim 1'$. Given that the median r_0 in the DGS sample is $\sim 0.6'$, it is thus important to take into account the contribution from the source falling outside the source aperture.

3.1.2. Computing the uncertainties

The uncertainties on the flux density arise from the non-systematic errors due to the measurement of the flux density on the maps, ($unc_{f_{tot}}$), and the systematic errors due to calibration, (unc_{calib}).

For the measurement on the maps, the system of equations being linear, the uncertainties arising from the two measurements on the map (unc_{ap} and unc_{bg}) can be linearly propagated to the total flux density and the background level, giving us the uncertainty on the total flux density ($unc_{f_{tot}}$) and the uncertainty on the background level (unc_b). The determination of unc_{ap} and unc_{bg} is the same for both errors as the measure is the same: summing pixels in a given region of the map. Thus we detail the calculation for unc_{ap} only.

There are two sources of errors to unc_{ap}: one coming from the sum of the pixels, unc_{sum}, one coming from the intrinsic error on the flux density value in each pixel, unc_{int}.

Determination of unc_{sum} : For each pixel there is a contribution from the background noise to the total measured flux density. This error, σ_{sky}, is the same for a pixel in the source aperture as well as in the background aperture, repeated N_{ap} times here. The error, σ_{sky}, is the standard deviation of all pixels in the background aperture. The final uncertainty, unc_{sum}, is then:

$$unc_{sum} = \sqrt{N_{ap}}\sigma_{sky} \quad (2)$$

Determination of unc_{int} : For each pixel there is an underlying uncertainty for the flux density value in the pixel, $\sigma_{int,i}$, and is independent from pixel to pixel. This uncertainty arises from the data reduction step when the flux density for each pixel is computed. A map of these uncertainties is produced during the data reduction process. The uncertainty, unc_{int}, is then derived by adding quadratically all of the errors in the considered pixels :

$$unc_{int} = \sqrt{\sum_{i=0}^{N_{ap}} \sigma_{int,i}^2} \quad (3)$$

Note that the assumption of pixel-to-pixel independent uncertainty is not applicable for PACS maps and this can result in an underestimation of unc_{int}.

The total error on the source aperture measurement is then :

$$unc_{ap} = \sqrt{unc_{sum}^2 + unc_{int}^2} \quad (4)$$

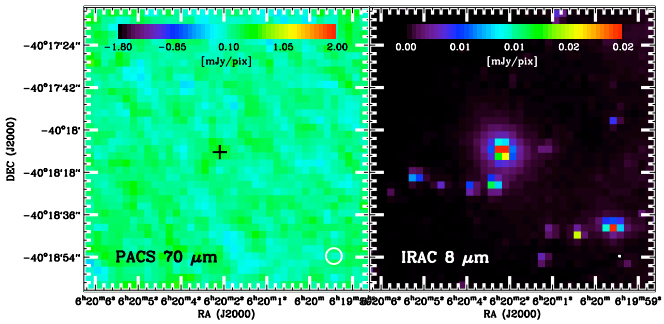

Fig. 3. Example of a PACS non-detection: (left) PACS 70 μm image of Tol 0618-402. The position of the galaxy is marked with a black cross. The IRAC 8 μm image has been added on the right for comparison. The PACS 70 μm (FWHM=5.6″) and the IRAC 8 μm (FWHM=2.0″) beams are indicated as white circles on the bottom right of the images.

The unc_{bg} is derived the same way and we can then compute $unc_{f_{tot}}$ and unc_b. The quantity $unc_{f_{tot}}$ is thus the total error on the flux density due to measurement on the map. To this uncertainty, we add in quadrature the systematic calibration uncertainty, unc_{calib}, of 5% for the three PACS bands (M. Sauvage & T. Müller, priv. com.), giving, in the end, the $\sigma_{70-100-160}$ reported in Table 2:

$$\sigma_\lambda = \sqrt{unc^2_{f_{tot}} + unc^2_{calib}} \quad (5)$$

Note that in unc_{sum}, we have a combination of uncertainties from small scale astronomical noise and instrumental uncertainties. These instrumental uncertainties can be redundant with part of the instrumental uncertainties taken into account in unc_{int}, leading to an overestimate of unc_{ap} and thus $unc_{f_{tot}}$. However, it has a minor impact on the final uncertainties, $\sigma_{70-100-160}$, as the calibration uncertainty is dominant.

3.1.3. Case of upper limits

Some galaxies in our sample are not detected in some or all of the PACS bands. We classify these galaxies as "upper limits" when the computed flux density is lower than five times the corresponding uncertainty on the flux density (e.g. Tol 0618-402, Figure 3). We take as the final upper limit, five times the uncertainty on the flux density value in order to have a 5σ upper limit (reported in Table 2).

3.2. SPIRE photometry

For the SPIRE photometre, the relative spectral response function (RSRF) is different for a point source or for an extended source. During the treatment by the pipeline, the measured RSRF-weighted flux density is converted to a monochromatic flux density for a source where ν*F$_\nu$ is constant, via the "K_4" correction defined in the SPIRE Observers' Manual (Section 5.2.7), assuming a *point-like* source. The output of the pipeline will be, by definition, a monochromatic flux density of a point source. To obtain monochromatic flux densities of extended sources we apply the ratio of K_4 corrections for extended and point-like sources, K_{4e}/K_{4p}, defined in the SPIRE Observers' Manual (Section 5.2.7). In order to determine which sources need this extra-correction, we have to distinguish between extended and point-like (unresolved) sources in our sample, as well as non-detected sources. Extended sources are defined as galaxies whose spatial extension is larger than the FWHM of the SPIRE beam, and non-detected sources are galaxies that are not visible at SPIRE wavelengths.

3.2.1. Extracting the fluxes

The photometry method is adapted for each type of galaxy. However, as the data reduction has been performed with HIPE v5, the 350 μm maps are first scaled by a factor of 1.0067 to update the maps to the latest version of the 350 μm flux calibration (SPIRE Observers' Manual (Section 5.2.8)).

Point source photometry

To determine the flux densities of point sources, we fit a Gaussian function (which is representative of the shape of the PSF) to the timeline data from the bolometres, using a timeline-based source fitter that is used for deriving the flux calibration for the individual bolometres[6]. We then check a posteriori that our "unresolved" classification was correct: if the FWHM of the fitted Gaussian is < 20″, 29″ and 37″ at 250, 350 and 500 μm respectively, then the source can be considered as truly point-like. As the timeline data is in Jy·beam^{-1}, the flux density will simply be the amplitude of the fitted Gaussian. This is the most accurate way of computing flux densities for point-like sources as it matches the measurement techniques used for the SPIRE calibration. Moreover we avoid all pixelization issues when using the timeline data rather than the map. On top of that, applying any mapmaking process would also smear the PSFs, causing the peak signal values to decrease by ~ 5% for point sources.

Extended source photometry

For the extended sources, we perform aperture photometry on the maps, using the same source and background apertures as those used for the PACS photometry, and check that the PACS apertures do fully encompass the SPIRE emission from the entire galaxy. The maps are converted from Jy·beam^{-1} to Jy·pix^{-1} considering that the beam area values are 465, 822 and 1768 square arcseconds[7] at 250, 350, 500 μm respectively and the pixel sizes are given in Section 2.2.3.

The background level is determined by the median of all of the pixels in the background aperture. The median is preferred rather than the mean because the SPIRE background is contaminated by prolific background sources due to some observations reaching the confusion limit. The background level is then subtracted from our maps and the total flux density is the sum of all of the pixels encompassed in the source aperture, corrected for K_{4e}/K_{4p}. These K_{4e}/K_{4p} correction factors, given in the SPIRE Observers' Manual (Section 5.2.8), are 0.98279, 0.98344 and 0.97099 at 250, 350, 500 μm respectively.

However there are also "marginally" extended sources (e.g. IIZw40) that do not require this K_{4e}/K_{4p} correction. To identify these sources, we first check that the source is truly resolved by applying the point source method on the timeline data. We verify that the FWHM is indeed greater than the chosen threshold val-

[6] The last version of this source fitter is incorporated into HIPE v10 (Bendo et al. in prep.).

[7] SPIRE photometre reference spectrum values: http://herschel.esac.esa.int/twiki/bin/view/Public/SpirePhotometerBeamProfileAnalysis, September 2012 values.

Table 2. Table of PACS flux densities for the DGS galaxies. The map making method is indicated for each galaxy as well as the radius of the circular aperture used for the flux extraction. When an upper limit is given, it is the 5σ upper limit computed in 3.1.3.

Source	F_{70} (Jy)	σ_{70} (Jy)	F_{100} (Jy)	σ_{100} (Jy)	F_{160} (Jy)	σ_{160} (Jy)	Method	Circular aperture radius ($''$)
Haro11	6.14	0.31	4.96	0.25	2.42	0.12	Scanamorphos	45[b]
Haro2	4.99	0.25	5.33	0.27	3.95	0.20	Scanamorphos	50[a]
Haro3	5.30	0.26	6.41	0.32	4.83	0.24	Scanamorphos	60[a]
He2-10	25.6	1.3	26.6	1.3	18.8	0.9	Scanamorphos	108[a]
HS0017+1055	0.046	0.005	0.033	0.004	0.019	0.004	PhotProject	16[b]
HS0052+2536	0.22	0.01	0.21	0.01	0.139	0.008	PhotProject	23[a,f]
HS0822+3542	≤ 0.014[j]	-	≤ 0.013[j]	-	0.034	0.003	PhotProject	12[a]
HS1222+3741	0.025	0.004	≤ 0.036	-	≤ 0.022	-	PhotProject	14[b]
HS1236+3937	≤ 0.029	-	≤ 0.035	-	≤ 0.028	-	PhotProject	15[a]
HS1304+3529	0.121	0.007	0.150	0.009	0.069	0.005	PhotProject	18[b]
HS1319+3224	0.012	0.003	0.013	0.002	≤ 0.015	-	PhotProject	8[b]
HS1330+3651	0.093	0.006	0.112	0.007	0.091	0.005	PhotProject	20[b]
HS1442+4250	0.09	0.01	≤ 0.016	-	≤ 0.047	-	PhotProject	51[a]
HS2352+2733	0.039	0.003	0.016	0.002	≤ 0.016	-	PhotProject	15[a]
IZw18	0.045	0.003	0.018	0.002	≤ 0.011	-	PhotProject	14[a]
IC10	140.	7.	207.	10.	225.	11.	Scanamorphos	306[a]
IIZw40	6.39	0.32	5.79	0.29	3.53	0.18	Scanamorphos	66[b]
Mrk1089	4.27	0.21	4.97	0.25	4.68	0.23	Scanamorphos	75[b,f]
Mrk1450	0.30	0.02	0.25	0.01	0.127	0.007	PhotProject	20[a]
Mrk153	0.28	0.02	0.30	0.02	0.137	0.009	PhotProject	35[b]
Mrk209	0.32	0.02	0.35	0.02	0.16	0.01	Scanamorphos	24[c]
Mrk930	1.19	0.06	1.40	0.07	0.98	0.05	Scanamorphos	60[b]
NGC1140	4.04	0.20	4.62	0.23	4.58	0.23	Scanamorphos	118[b]
NGC1569	60.4	3.0	57.3	2.9	39.7	2.0	Scanamorphos	150[d]
NGC1705	1.37	0.07	1.46	0.07	1.10	0.06	PhotProject[g]	72[d]
NGC2366	5.30	0.26	6.23	0.31	4.08	0.20	Scanamorphos	150[d,e]
NGC4214	24.5	1.2	32.2	1.6	33.7	1.7	Scanamorphos	300[d]
NGC4449	49.3	2.5	75.9	3.8	79.5	4.0	Scanamorphos	250[d]
NGC4861	2.31	0.12	2.17	0.11	1.99	0.10	Scanamorphos	120[d]
NGC5253	32.9	1.6	32.3	1.6	23.2	1.2	Scanamorphos	120[d]
NGC625	6.49	0.32	9.47	0.47	8.20	0.41	Scanamorphos	170[d]
NGC6822	54.9	2.8	63.6	3.2	77.1	3.9	Scanamorphos	440[d]
Pox186	0.038[j]	0.005	0.052[j]	0.005	0.047[j]	0.004	PhotProject	16[a]
SBS0335-052	0.056	0.004	0.024[h]	0.001	0.007[h]	0.001	PhotProject	10[a,h]
SBS1159+545	0.019	0.003	0.019	0.003	≤ 0.018	-	PhotProject	8[a]
SBS1211+540	0.034	0.003	0.018	0.002	0.013	0.002	PhotProject	15[b]
SBS1249+493	0.032	0.005	≤ 0.034	-	≤ 0.042	-	PhotProject	12[b]
SBS1415+437	0.18	0.01	0.16	0.01	0.065	0.007	PhotProject	34[a]
SBS1533+574	0.19	0.01	0.24	0.01	0.19	0.01	Scanamorphos	30[a]
Tol0618-402	≤ 0.014	-	≤ 0.005	-	≤ 0.013	-	PhotProject	18[a]
Tol1214-277	0.017	0.003	0.018	0.002	≤ 0.018	-	PhotProject	12[b]
UGC4483	0.16	0.02	-[i]	-[i]	≤ 0.037	-	PhotProject	63[a]
UGCA20	≤ 0.052	-	≤ 0.057	-	≤ 0.048	-	PhotProject	20[c]
UM133	0.15[j]	0.01	0.066	0.010	0.053	0.009	Scanamorphos	26[c]
UM311	2.94	0.15	5.63	0.28	6.10	0.31	Scanamorphos	140[b,f]
UM448	5.17	0.26	-	-	3.22	0.17	Scanamorphos	64[b]
UM461	0.21[j]	0.01	0.145	0.009	0.113	0.007	PhotProject	17[b]
VIIZw403	0.47	0.03	0.56	0.03	0.34	0.02	PhotProject	40[c]

[a,b,c]: The radius is: [a]: 1.5 times the optical radius. [b]: larger than 1.5 times the optical radius. [c]: smaller than 1.5 times the optical radius.
[d,e]: The aperture is: [d]: adapted from elliptical shape. [e]: off-centred to match the particular shape of the galaxy.
[f]: These objects are galaxies within compact groups of galaxies or are parts of other galaxies and the photometry given here is for the whole group (see Section 3.1.1 for details).
[g]: The Scanamorphos maps of NGC1705 are not satisfactory because of a non-uniform background. Therefore we use the PhotProject maps. To preserve as much of the diffuse extended emission as possible we manually mask out the galaxy before performing the high-pass filtering step.
[h]: New observations were obtained for SBS0335-052 at 100 and 160 μm with longer integration times (Sauvage et al. in prep). We chose to quote the flux density values from the newest observations for 100 and 160 μm.
[i]: Interferences on the detector are strongly polluting the map for the 100 μm observation of UGC4483. We thus do not report any flux density nor give any 100 μm map for this galaxy.
[j]: These flux densities might present some discrepancies with other FIR measurements (i.e. MIPS, other PACS and/or SPIRE wavelengths).

ues for the "unresolved" classification. As an additional check, the fitted Gaussian is subtracted from the map and the resulting map is visually checked for any remaining emission from the source. If this condition is satisfied, then the source is truly resolved. If the FWHM of the fitted Gaussian is lower than $24''$, $34''$ and $45''$ at 250, 350, 500 μm respectively then the source is considered to be "marginally" extended only, and thus to not require the K_{4e}/K_{4p} correction.

3.2.2. Computing the uncertainties

As for the PACS photometry, there are two types of uncertainties for SPIRE photometry: the errors arising from the determination of the flux density, unc_{flux}, and the calibration errors, unc_{calib}. As we used different methods for flux extraction depending on the type of the source, the errors contributing to unc_{flux} are determined differently. The method described here has been adapted from the method described in Ciesla et al. (2012).

Point source photometry

The uncertainty on the flux density for a point source is determined through a test in which we add 100 artificial sources with the same flux density as the original source. They are added at random locations in the map, within a 0.3 deg box centred on the original source. The same photometry procedure was applied to the artificial sources and the final uncertainty is the standard deviation in the flux densities derived for the artificial sources. We quote the following uncertainties (unc_{flux}) for point-like sources:

- 6 mJy at 250 μm;
- 7 mJy (for flux densities > 50 mJy) and 10 mJy (for flux densities $\lesssim$ 50 mJy) at 350 μm;
- 9 mJy at 500 μm.

Extended source photometry

For the aperture photometry performed on the extended sources, we have three types of uncertainties contributing to unc_{flux}: the uncertainty arising from the background level determination, unc_{bg}, the uncertainty due to background noise in the source aperture, unc_{source}, the underlying uncertainty for the flux density value in the pixel coming from the data reduction, unc_{int}, and the uncertainty in the beam area value: unc_{beam}, which is given to be 4%[8].

The determination of the background level generates an uncertainty which will affect each pixel in the source aperture when subtracting the background level from the map. The uncertainty on the background level is $unc_{bg_{level}} = \sigma_{sky}/\sqrt{N_{bg}}$, with σ_{sky} being here again the standard deviation of all of the pixels in the background aperture. This will affect the determination of the flux density for each pixel summed in the aperture :

$$unc_{bg} = N_{ap} unc_{bg_{level}} \quad (6)$$

The uncertainty due to background noise in the source aperture, unc_{source}, is determined the same way as the PACS unc_{ap} since it is the uncertainty arising from summing the pixels in a given aperture :

$$unc_{source} = \sqrt{N_{ap}}\sigma_{sky} \quad (7)$$

The uncertainty arising from the underlying uncertainties of the flux density value in each pixel is computed the same way as for PACS. Here again, this uncertainty arises from the data reduction step when the flux density for each pixel is computed, and the pipeline produces the corresponding error map :

$$unc_{int} = \sqrt{\sum_{i=0}^{N_{ap}} \sigma_{int,i}^2} \quad (8)$$

[8] This value is given in: http://herschel.esac.esa.int/twiki/bin/view/Public/SpirePhotometerBeamProfileAnalysis.

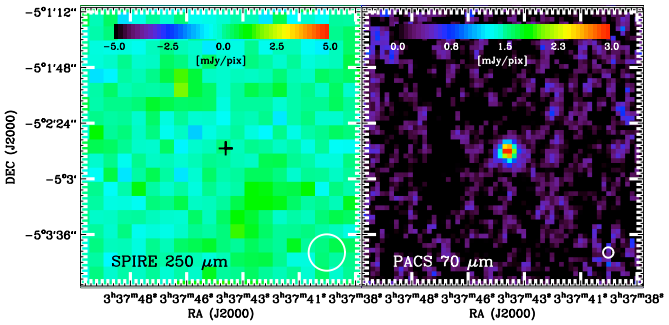

Fig. 4. Example of a SPIRE non-detection: (left) SPIRE 250 μm and (right) PACS 70 μm image of SBS 0335-052. The position of the galaxy is indicated by a black cross on the SPIRE image. The SPIRE 250 μm (FWHM=18.2″) and the PACS 70 μm (FWHM=5.6″) beams are indicated as white circles on the bottom right of the images.

The total uncertainty coming from the determination of the flux density for an extended source, is then :

$$unc_{flux} = \sqrt{unc_{bg}^2 + unc_{source}^2 + unc_{int}^2 + unc_{beam}^2} \quad (9)$$

For both types of sources, we also add calibration uncertainties to unc_{flux} to get the final total uncertainty. There are two different SPIRE calibration uncertainties: a systematic uncertainty of ~ 5% coming from the models used for Neptune, the primary calibrator, which is correlated between the three bands, and a random uncertainty of ~ 2% coming from the repetitive measurement of the flux densities of Neptune. These two uncertainties were added linearly instead of in quadrature as advised in the SPIRE Observer's Manual, giving an overall 7% calibration uncertainty unc_{calib}. The final total uncertainty, $\sigma_{250-350-500}$ reported in Table 3, is obtained by adding unc_{flux} and unc_{calib} in quadrature.

As for PACS, with SPIRE we also have a redundancy in the error estimation in unc_{source} and unc_{int}, again with only a minor impact on the final uncertainties, $\sigma_{250-350-500}$, as the calibration uncertainty dominates.

3.2.3. Case of upper limits

When the galaxy is not detected in the SPIRE bands (e.g. SBS 0335-052, Figure 4), we can only derive upper limits on the flux density. Also, when the source is blended with another source in the beam and we are unable to confidently separate them (e.g. Pox186 and a background galaxy separated by 20″, Figure 5), upper limits are reported. Since the undetected sources are point sources, we use five times the uncertainties reported for point sources in 3.2.2. The only exception is SBS1533+574 which is blended with another source and slightly extended at 250 μm. The method described above gives an upper limit too low. The extended source photometry method is thus used to derive a 5σ upper limit at this wavelength.

3.2.4. Special cases: heavy cirrus contamination

For NGC 6822 and IC 10, the cirrus contamination from our Galaxy is important in the SPIRE bands.

NGC 6822 - Galametz et al. (2010) determined that the contribution from the cirrus to the total emission of the galaxy is of

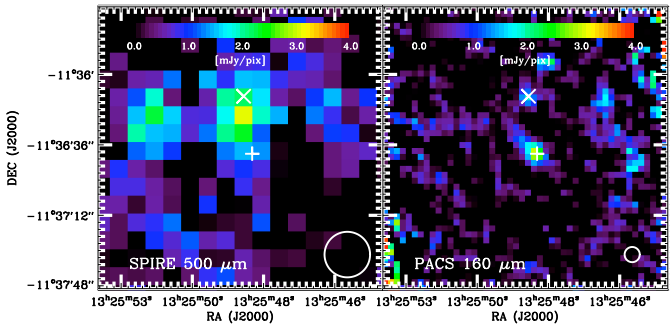

Fig. 5. Example of a "mixed" source. SPIRE 500 μm (left) and PACS 160 (right) images of Pox186 and a contaminating background source. The sources are 20″ apart, and are well separated at 160 μm, but are completely blended at SPIRE 500 μm resolution. Pox186 corresponds to the bottom cross, whereas the contaminating background source is the X. The SPIRE 500 μm (FWHM=36.3″) and the PACS 160 μm (FWHM=11.3″) beams are indicated as white circles on the bottom right of the images.

the order of 30% for all SPIRE bands. To determine the cirrus contribution here, we assume that the entire galaxy is in a homogeneous and flat cirrus region. We determine this cirrus level by considering regions at the same cirrus level outside of the galaxy. This level is used as the background level for the flux determination. We then compare this flux density with the flux density obtained when we consider an uncontaminated background region and get the contamination from the cirrus. We also find that the contribution of the cirrus to the total flux densities is about 30%, which is coherent with the results from Galametz et al. (2010). Thus for this galaxy, the flux densities cited in Table 3 are flux densities where the cirrus contribution has been subtracted. We also include a conservative 30% uncertainty in the error for these flux densities to account for the estimation of the cirrus contribution, and for the fact that the cirrus emission may not be flat.

IC 10 - We apply the same method here. Again, we find that the cirrus contributes ~ 30% on average, to each SPIRE band. We took this contribution into account by adding this cirrus uncertainty to the other sources of uncertainties for this galaxy.

This method can be improved, by using the HI maps to better determine the cirrus emission and the background level and thus reducing the uncertainties on the measurements for these two galaxies.

3.3. Comparison of PACS and MIPS existing flux densities

We compare our PACS flux densities to the flux densities at 70 and 160 μm from MIPS onboard the *Spitzer* Space Telescope from Bendo et al. (2012) to assess the reliability of our measurements.

3.3.1. MIPS photometry

The table of the available MIPS data for the DGS is given in Madden et al. (2013) and Bendo et al. (2012) who give a detailed description of the photometry for total galaxy flux densities. Of the DGS sample, 34 galaxies have been observed by MIPS in the considered bands. Bendo et al. (2012) MIPS flux densities compare well with previously published MIPS samples containing a subset of the DGS galaxies (Dale et al. 2007; Engelbracht et al. 2008). Therefore we are confident about the reliability of these results and will use them to perform the comparison with our PACS flux densities.

3.3.2. Comparison with PACS

The PACS flux densities correspond to monochromatic values for sources with spectra where νf_ν is constant, while the MIPS flux densities are monochromatic values for sources with the spectra of a 10^4 K blackbody, so colour corrections need to be applied to measurements from both instruments before they are compared to each other. We first fit a blackbody through the three PACS data points and apply the corresponding colour corrections from the available PACS documentation[9]. For the MIPS flux densities, we fit a blackbody through the 70 and 160 μm data points (not using the 24 μm point) and apply the corrections from the MIPS Handbook[10]. The typical colour corrections for MIPS are of the order of 10 and 4% on average at 70 and 160 μm. However, they are of the order of 1 or 2% in the 70 and 160 μm PACS bands. For non detected galaxies, where we, for PACS, and/or Bendo et al. (2012), for MIPS, reported upper limits (nine galaxies), we are not able to properly fit a blackbody and therefore derive a proper colour correction. We do not compare PACS and MIPS flux densities for these galaxies for now.

We use the ratios of the PACS and MIPS flux densities to assess how well the measurements from the instrument agree with each other; a ratio of one corresponds to a very good agreement. The average PACS/MIPS ratios at 70 and 160 microns are shown in Figure 6, and the correspondence is relatively good. The PACS/MIPS ratio is 1.019 ± 0.112 at 70 μm and 0.995 ± 0.153 at 160 μm. This is to be compared to an average uncertainty of ~12% (~11% from MIPS and ~5% for PACS, added in quadrature) and ~16% (~15% from MIPS and ~7% for PACS, added in quadrature) on the ratios at 70 and 160 μm respectively. Aniano et al. (2012) found a slightly less good agreement (~ 20%) for integrated fluxes of two KINGFISH galaxies.

If we now consider galaxies detected at 70 μm and not at 160 μm, indicated by a different symbol on the upper panel of Figure 6, we are still able to compare, with extra caution, the measurements at 70 μm. Indeed, as we are not able to derive a proper colour correction for those galaxies, we add to the MIPS 70 μm flux densities a 10% uncertainty and a 1% uncertainty to the PACS 70 μm flux densities to account for the colour correction effect. When adding these extra galaxies at 70 μm, the PACS/MIPS ratio is 0.985 ± 0.158 at 70 μm. This is to be compared with an average uncertainty of ~14% on the 70 μm ratio (~12% from MIPS and ~7% for PACS, added in quadrature, including the extra galaxies). The very faint and discrepant galaxies at 70 μm are HS1222+3741 (ratio of 0.40) and Tol1214-277 (ratio of 0.24). For HS1222+3741, the MIPS image contains some bright pixels near the edge of the photometry aperture used for MIPS, and this may have driven the 70 μm MIPS flux density up. For Tol1214-277, a nearby source is present in the MIPS data and, although its contribution has been subtracted when computing the MIPS 70 μm flux, some contribution from this source may still be present. Additionally, measuring accurate flux densities at ≤ 50 mJy in both MIPS and PACS data is difficult and may have led to the discrepancies.

[9] The corresponding documentation for PACS colour corrections is available at http://herschel.esac.esa.int/twiki/pub/Public/PacsCalibrationWeb/cc_report_v1.pdf

[10] The MIPS Instrument Handbook is available at http://irsa.ipac.caltech.edu/data/SPITZER/docs/mips/mipsinstrumenthandbook/home/

Table 3. Table of SPIRE flux densities for the DGS galaxies. When an upper limit is given, it is the 5σ upper limit computed in 3.2.3.

Source	F_{250} (Jy)	σ_{250} (Jy)	F_{350} (Jy)	σ_{350} (Jy)	F_{500} (Jy)	σ_{500} (Jy)
Haro11	0.63	0.05	0.23	0.02	0.09	0.01
Haro2	1.28[a]	0.10	0.53[a]	0.04	0.15[a]	0.01
Haro3	1.79[a]	0.15	0.77[a]	0.07	0.23[a]	0.02
He2-10	6.67[a]	0.54	2.64[a]	0.22	0.79[a]	0.07
HS0017+1055	≤0.030	-	≤0.050	-	≤0.045	-
HS0052+2536[b]	0.058	0.007	0.03	0.01	0.018	0.009
HS0822+3542[c]	-	-	-	-	-	-
HS1222+3741[c]	-	-	-	-	-	-
HS1236+3937	≤0.030	-	≤0.050	-	≤0.045	-
HS1304+3529	0.038	0.007	≤0.050	-	≤0.045	-
HS1319+3224[c]	-	-	-	-	-	-
HS1330+3651[c]	-	-	-	-	-	-
HS1442+4250	≤0.030	-	≤0.050	-	≤0.045	-
HS2352+2733	≤0.030	-	≤0.050	-	≤0.045	-
IZw18	≤0.030	-	≤0.050	-	≤0.045	-
IC10[d]	101.[a]	31.	47.6[a]	14.8	16.3[a]	5.1
IIZw40	1.33[a]	0.12	0.58[a]	0.06	0.18	0.02
Mrk1089[b]	1.75[a]	0.15	0.78[a]	0.07	0.24[a]	0.03
Mrk1450	0.049	0.007	≤0.050	-	≤0.045	-
Mrk153	0.048[a]	0.008	≤0.050	-	≤0.045	-
Mrk209	0.062	0.007	0.03	0.01	≤0.045	-
Mrk930	0.40[a]	0.04	0.13[a]	0.01	0.049[a]	0.007
NGC1140	1.97[a]	0.17	0.94[a]	0.08	0.28[a]	0.03
NGC1569	12.0[a]	1.0	5.02[a]	0.41	1.55[a]	0.13
NGC1705	0.60[a]	0.05	0.29[a]	0.03	0.10[a]	0.01
NGC2366	2.04[a]	0.17	1.01[a]	0.09	0.39[a]	0.04
NGC4214	18.6[a]	1.5	9.92[a]	0.80	3.79[a]	0.31
NGC4449	32.4[a]	2.6	14.8[a]	1.2	5.01[a]	0.41
NGC4861	1.10[a]	0.10	0.54[a]	0.05	0.20[a]	0.03
NGC5253	7.82[a]	0.63	3.64[a]	0.29	1.18[a]	0.10
NGC625	4.33[a]	0.35	2.18[a]	0.18	0.80[a]	0.07
NGC6822[d]	48.4[a]	15.0	29.7[a]	9.2	13.6[a]	4.2
Pox186	0.045	0.007	≤0.050	-	≤0.045	-
SBS0335-052	≤0.030	-	≤0.050	-	≤0.045	-
SBS1159+545	≤0.030	-	≤0.050	-	≤0.045	-
SBS1211+540	≤0.030	-	≤0.050	-	≤0.045	-
SBS1249+493	≤0.030	-	≤0.050	-	≤0.045	-
SBS1415+437[c]	-	-	-	-	-	-
SBS1533+574	≤0.122[a]	-	≤0.050	-	≤0.045	-
Tol0618-402[c]	-	-	-	-	-	-
Tol1214-277	≤0.030	-	≤0.050	-	≤0.045	-
UGC4483	0.024	0.006	≤0.050	-	≤0.045	-
UGCA20[c]	-	-	-	-	-	-
UM133	0.032	0.006	≤0.050	-	≤0.045	-
UM311[b]	3.84[a]	0.31	1.87[a]	0.16	0.66[a]	0.06
UM448	0.99[a]	0.08	0.38[a]	0.03	0.13	0.01
UM461	0.027	0.006	0.03	0.01	≤0.045	-
VIIZw403	0.14[a]	0.01	0.053	0.008	0.028	0.009

[a]: The flux densities are derived from aperture photometry, with the same aperture used for PACS.
[b]: These objects are galaxies within compact groups of galaxies or are parts of other galaxies and the photometry given here is for the whole group (see Section 3.1.1 for details).
[c]: These sources were not observed at all by SPIRE.
[d]: The quoted flux densities for these sources have been corrected for cirrus contamination.

The error on the average ratio is comparable to the average uncertainties on the ratio for both bands. Thus there is a good photometric agreement between PACS and MIPS photometry for the DGS sample.

4. Far Infrared and submillimetre behaviour and dust properties of the dwarf galaxies

To study the dust properties of the DGS and determine the impact of metallicity, we perform a comparison with galaxies from the KINGFISH sample (Kennicutt et al. 2011). The KINGFISH survey contains 61 galaxies: 41 spiral galaxies, 11 early-type galaxies (E and S0) and nine irregulars (Kennicutt et al. 2011). KINGFISH is a survey including more metal-rich galaxies and enables us to span a wider metallicity range, notably by filling

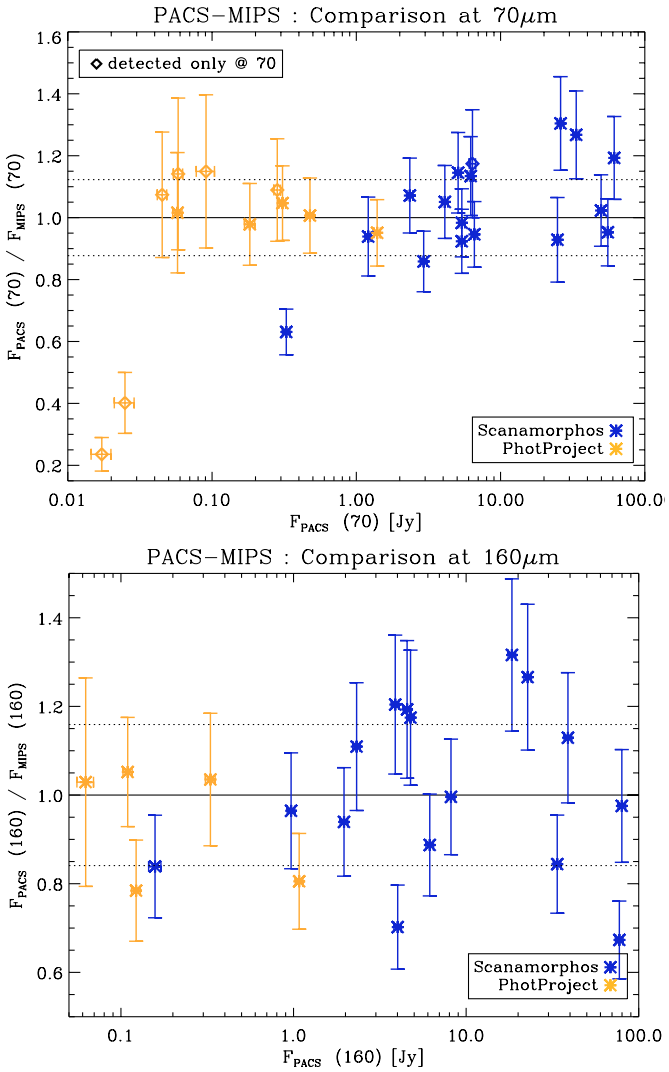

Fig. 6. Comparison of PACS flux densities and MIPS flux densities: PACS-to-MIPS flux density ratios as a function of PACS flux density at 70 μm *(top)* and 160 μm *(bottom)*. As a guide to the eye, the unity line is added as a solid line as well as the average uncertainties on the ratio in both bands as dotted lines. These average uncertainties are ~12% and ~16% at 70 and 160 μm. Colours distinguish the selected mapping method.

up the high-metallicity end of the metallicity distribution (Fig. 7). The metallicities adopted here for the KINGFISH sample have been determined the same way as for the DGS in Kennicutt et al. (2011), using the method of Pilyugin & Thuan (2005)[11]. No errors for metallicities are given in Kennicutt et al. (2011) so we adopt a 0.1 dex error for the KINGFISH metallicities. The *Herschel* KINGFISH flux densities are taken from Dale et al. (2012)[12].

We use FIR colour-colour diagrams (Section 4.1) and modified blackbody models (Section 4.2) in order to derive some

[11] See Madden et al. (2013) for the DGS metallicity determination. The KINGFISH metallicities are from Column 9 from Table 1 of Kennicutt et al. (2011).

[12] The KINGFISH SPIRE fluxes and corresponding uncertainties are updated to match the latest SPIRE beam areas. The beam areas used in this paper were released in September 2012, after the publication of Dale et al. (2012) in January 2012.

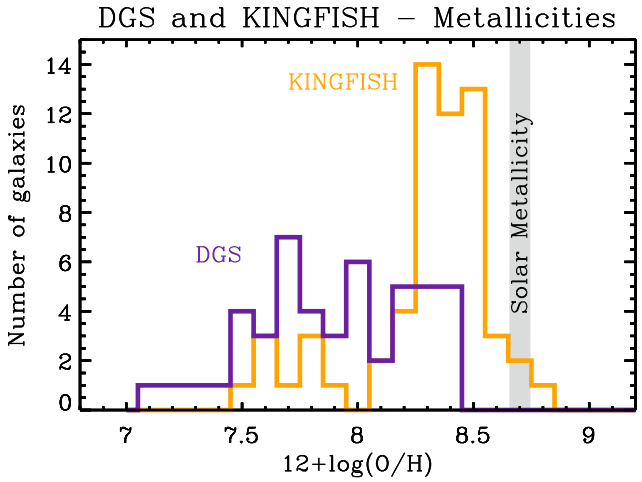

Fig. 7. Metallicity distributions for both DGS (purple) and KINGFISH (orange) samples. Note how the high-metallicity end is better covered by KINGFISH whereas the low-metallicity end is better covered by the DGS.

physical dust parameters of the galaxies, such as the temperature (T), the emissivity index (β), the dust mass (M_{dust}) and the FIR luminosity (L_{FIR}). In Section 4.3, we then investigate the presence of a possible submm excess in the galaxies .

4.1. Characterization of the SED shapes

In order to obtain a qualitative view of the FIR-to-submm behaviour of the DGS sample, and to compare with the KINGFISH sample, we inspect the observed *Herschel* SEDs as well as several *Herschel* colour-colour diagrams combining both PACS and SPIRE observations.

4.1.1. Observed spectral energy distributions

Total observed SEDs for both samples are computed for a first look at the characteristic SED shapes in the DGS and KINGFISH samples (Figure 8). The upper limits are not indicated here for clarity. The most metal-poor galaxies are also the faintest and therefore not detected with *Herschel* beyond 160 μm. The observed SEDs are normalized at 70 μm, and we see here that the peak of the SED shifts towards longer wavelengths as the metallicity increases, reflecting the impact of metallicity on the observed dust properties.

4.1.2. Dwarf Galaxy Survey colours

Constructing the colour-colour diagrams

The *Herschel* colour-colour diagrams are constructed first by computing the observed ratios and the corresponding error bars, for both DGS and KINGFISH, and omitting the galaxies with more than one upper limit in the considered bands.

We then compute the theoretical *Herschel* flux ratios of simulated modified blackbodies spanning a range in temperature (T from 0 to 40 K in 2 K bins and from 40 to 100 K in 10 K bins) and emissivity indices (β from 0.0 to 2.5). From now on, we define the emissivity index fixed for modelling the simulated *Herschel* flux ratios as "β_{theo}", and "β_{obs}" when we leave the emissivity

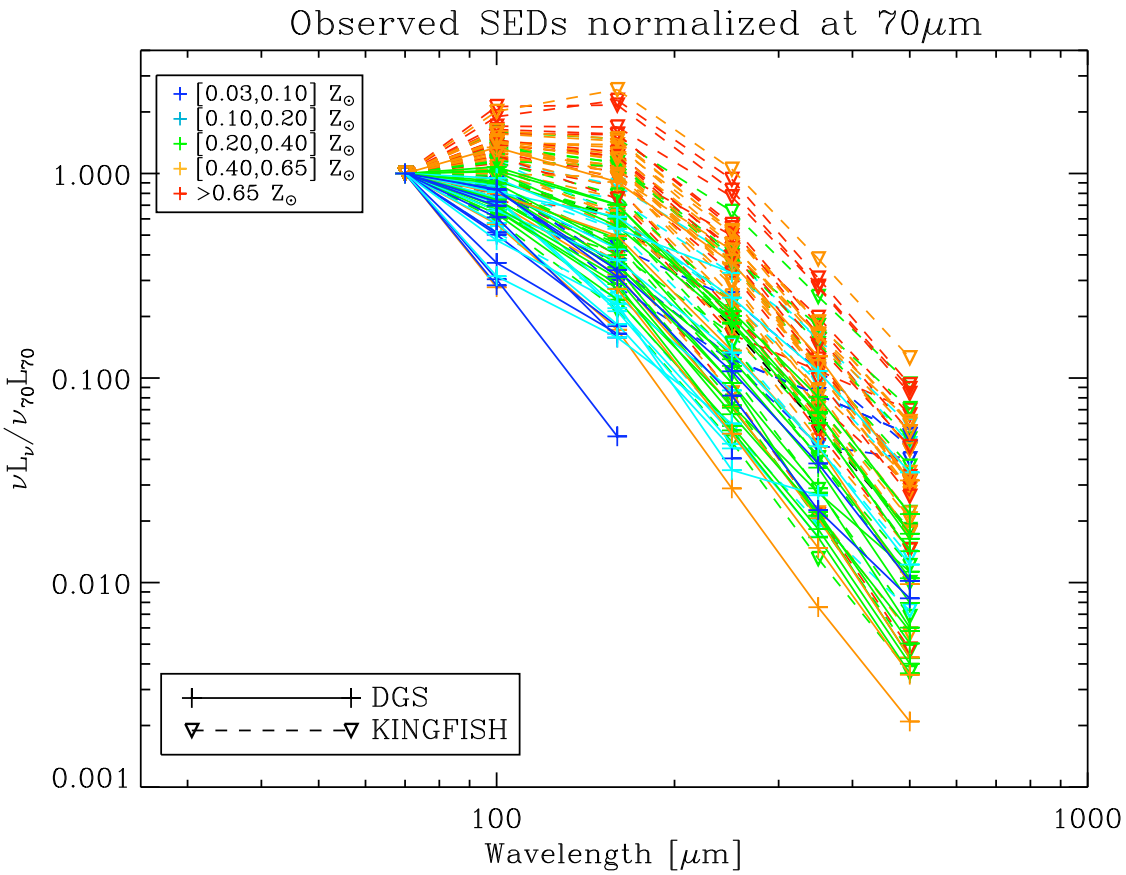

Fig. 8. Total *Herschel* observed SEDs for both DGS and KINGFISH samples, normalized at 70 μm. The colours delineate the different metallicity bins, and the lines and symbols differentiate DGS (plain lines and crosses) and KINGFISH galaxies (dashed lines and downward triangles).

index as a free parameter in modified blackbody fits (see Section 4.2). In our simulated modified blackbody, the emitted fluxes are proportional to $\lambda^{-\beta_{theo}} \times B_\nu(\lambda, T)$, where $B_\nu(\lambda, T)$ is the Planck function.

The pipeline we use for the data reduction gives us monochromatic flux densities for our data points for both PACS and SPIRE. To mimic the output of the pipeline for our theoretical points we weigh our theoretical flux density estimates by the RSRF of the corresponding bands. For SPIRE simulated measurements, we then convert our RSRF-weighted flux densities into monochromatic flux densities by applying the K_4 correction given on the SPIRE Observers' Manual. For PACS, we also colour correct the RSRF-weighted modeled flux densities to a spectrum where νF_ν is constant (i.e. multiply by the analogous of K_4 for PACS). These simulated flux ratios from a simple model are useful indicators to interpret the colour-colour diagrams.

FIR/submm colours

The spread of galaxies on the colour-colour diagrams (Figures 9 and 10) reflects broad variations in the SED shape and metallicity in our survey.

Indeed the DGS galaxies show a wider spread in location on the diagrams compared to the KINGFISH galaxies (Figures 9 and 10, top panels), reflecting the differences in the dust properties between dwarf galaxies and the generally more metal-rich environments probed by the KINGFISH survey.

The F_{70}/F_{100} *vs* F_{100}/F_{160} diagram (Figure 9) traces best the peak of the SED. Galaxies usually exhibit a peak in their SED around ~ 100 - 160 μm. Galaxies presenting FIR flux densities with $F_{70} > F_{100} > F_{160}$ may be quite warm as they peak at wavelengths less than 70 μm. Colder galaxies would lie in the lower left corner of the plot ($F_{70} < F_{100} < F_{160}$), as shown by the simulated flux ratio lines. KINGFISH galaxies indeed cluster in the corresponding lower left corner of the plot while DGS galaxies span a wider space (Fig 9, top). Nonetheless both samples follow the theoretical flux ratio lines from simulated modified blackbodies. There are some outliers, all of them being very faint, extremely metal-poor galaxies (from 0.03 to 0.20 $Z_\odot$). There is also a metallicity trend in Fig. 9 (bottom), either between KINGFISH and the DGS or within both samples, i.e. low-metallicity (dwarf) galaxies peak at much shorter wavelengths and thus have overally warmer dust (several tens of K), compared to more metal-rich galaxies.

In dwarf galaxies, the warmer dust is due to the very energetic environment in which the grains reside: the density of young stars causes the ISRF to be much harder on global scales than in normal galaxies (Madden et al. 2006). The low dust extinction enables the FUV photons from the young stars to penetrate deeper into the ISM. The dust grains are thus exposed to harder and more intense ISRF than in a more metal-rich environment. This increases the contribution of hot and warm dust

to the total dust emission resulting in overall higher equilibrium dust temperatures.

Note that there is a small excess at 70 μm for most of the galaxies compared to our simulated modified blackbodies, causing them to fall above the lowest β_{theo} line. This means that if we were to fit a modified blackbody *only* to the FIR flux densities (from 70 μm to 160 μm) we would get very low β_{obs}, i.e. a very flat SED in the FIR, which reflects a broad peak in the observed SED. This is due to the crudeness of the isothermal approximation made in the modified blackbody modelling. In a real galaxy, the dust grains are distributed in a range of temperatures, (e.g. hotter dust around star-forming regions vs colder dust in the diffuse ISM). Such a low β_{obs} here is only a side effect of the distribution in temperature of the grains in the galaxy. The extremely metal-poor outliers noted before may present an even wider temperature distribution than in more metal-rich galaxies, towards the higher temperatures, causing the broadening of the peak in their dust SED and their peculiar location on the diagrams in Fig. 9. Part of this excess at 70 μm could also be due to non-thermal heating, i.e. dust grains whose emission can not be represented by a modified blackbody, such as stochastically heated small grains.

More accurate values of T and β_{theo} may be illustrated by including submm data in the colour-colour diagrams. At submm wavelengths (beyond $\sim$ 250 μm), the emissivity index this time represents an intrinsic grain property: the efficiency of the emission from the dust grain. A theoretical emissivity index $\beta_{theo} = 2$ is commonly used to describe the submm SED for local and distant galaxies in the models as it represents the intrinsic optical properties of Galactic grains (mixture of graphite and silicate grains). More recently β_{theo} between 1.5 and 2 have also been used (e.g. Amblard et al. 2010; Dunne et al. 2011). The F_{100}/F_{250} *vs* F_{250}/F_{500} diagram (Figure 10) reflects best the variations in emissivity index β_{theo}. Here again the DGS galaxies are more wide-spread than the KINGFISH galaxies (Figure 10, top) spanning larger ranges of F_{100}/F_{250} and F_{250}/F_{500} ratios, that is, wider ranges in temperature and β (such as higher T and lower β). As far as metallicity is concerned, the trend with temperature already noted in Fig. 9 is still present (Figure 10, bottom). But hardly any trend between β and metallicity can be noticed: as the extremely low-metallicity galaxies are not detected at 500 μm, it is rather difficult to conclude on this point relying only on the FIR/submm colour-colour diagram.

Modelling low-metallicity dwarf galaxies with grain properties derived from the Galaxy (i.e. using β_{theo} =2), may thus not be accurate. The galaxies showing a lower β_{obs} ($\beta_{obs} < 2$) will have a flatter submm slope. Smaller F_{250}/F_{500} ratios, that can be seen as a sign of lower β_{obs}, indicative of a flatter submm slope, have already been noted by Boselli et al. (2012) for sub-solar metallicity galaxies. This flatter slope may be the sign of a contribution from an extra emission in excess of the commonly used β_{theo} = 2 models. Thus the flattening of the observed submm slope (β_{obs} < 2) could be used as a diagnosis for possible excess emission appearing at 500 μm (see Section 4.3).

4.2. FIR/Submm modelling

To complete our observational and qualitative view of the FIR-submm behaviour of the DGS and KINGFISH galaxies, we use a modified blackbody model to quantitatively determine the parameters already discussed before: L_{FIR}, M_{dust}, T, β_{obs}, in the DGS and KINGFISH samples.

4.2.1. Modified blackbody fitting

A single modified blackbody is fitted to the *Herschel* data of each galaxy from the DGS sample where the free parameters are: temperature (T) and dust mass (M_{dust}) as well as the emissivity index (β_{obs}), where we leave β_{obs} free in the [0.0, 2.5] range. The modeled flux densities are given by:

$$F_\nu(\lambda) = \frac{M_{dust}\kappa(\lambda_0)}{D^2}\left(\frac{\lambda}{\lambda_0}\right)^{-\beta_{obs}} B_\nu(\lambda, T) \quad (10)$$

where $\kappa(\lambda_0) = 4.5\ m^2 kg^{-1}$ is the dust mass absorption opacity at the reference wavelength, λ_0 = 100 μm. $\kappa(\lambda_0)$ has been calculated from the grain properties of Zubko et al. (2004), as in Galliano et al. (2011)[13], and is consistent with a β_{theo} = 2. Leaving β_{obs} to vary in our fit can produce lower dust masses for lower β_{obs} (Bianchi 2013). This effect is discussed for the two dust masses relations we derive in Section 4.2.3. Moreover, this particular choice for the value $\kappa(\lambda_0)$ will only affect the absolute values of the dust masses. Choosing another model to derive $\kappa(\lambda_0)$ would not affect the intrinsic variations noted in Section 4.2.3. D is the distance to the source (given in Table 1) and $B_\nu(\lambda, T)$ is the Planck function. Colour corrections are included in the fitting procedure.

At 70 μm, possible contamination by dust grains that are not in thermal equilibrium, and whose emission cannot be represented by a modified blackbody, can occur in galaxies. An excess at 70 μm compared to a modified blackbody model can also appear, as seen in Fig. 9, because dust grains in a galaxy are more likely to have a temperature distribution rather than a single temperature. For example in spiral galaxies (present in the KINGFISH sample), the dust emitted at 70-500 μm can originate from two components with different heating sources and potentially different temperatures (Bendo et al. 2010, 2012; Boquien et al. 2011; Smith et al. 2012b). Therefore, we restrict our wavelength fitting range to 100 - 500 μm. The 70 μm point can be useful as an upper limit for a single temperature dust component. We redo the fit including the 70 μm point only if the modelled point from the fit without 70 μm data violates this upper limit condition, i.e. if it is greater than the observed point (e.g. Mrk 209 in Figure 11).

Some of our galaxies are not detected at some wavelengths. To have enough constraints for the fit, at least a detection up to 250 μm is required. If the galaxy is not detected beyond 160 μm, we fit a modified blackbody including the 70 μm point. Indeed some galaxies peaking at very short wavelengths have their Rayleigh Jeans contribution dropping at FIR and submm wavelengths, and are often not detected by SPIRE. For these galaxies, the 70 μm point is already on the Rayleigh Jeans side of the modified blackbody, and in this case we also include it in our fit.

All of these conditions are matched for 35 galaxies, and we use the 70 μm point for 11 of them (five because of the violation of the upper limit condition at 70 μm, four because the galaxy is not detected beyond 160 μm, and two because the galaxy is not observed by SPIRE, see Table 4 for details).

From the fitted modified blackbodies, we also derive the total FIR luminosity, L_{FIR}, by integrating the modelled curve between 50 and 650 μm. The resulting parameters from the fits are given in Table 4. The SEDs are shown in Appendix A for all 35 DGS galaxies.

[13] for their "Standard Model", see Appendix A of Galliano et al. (2011).

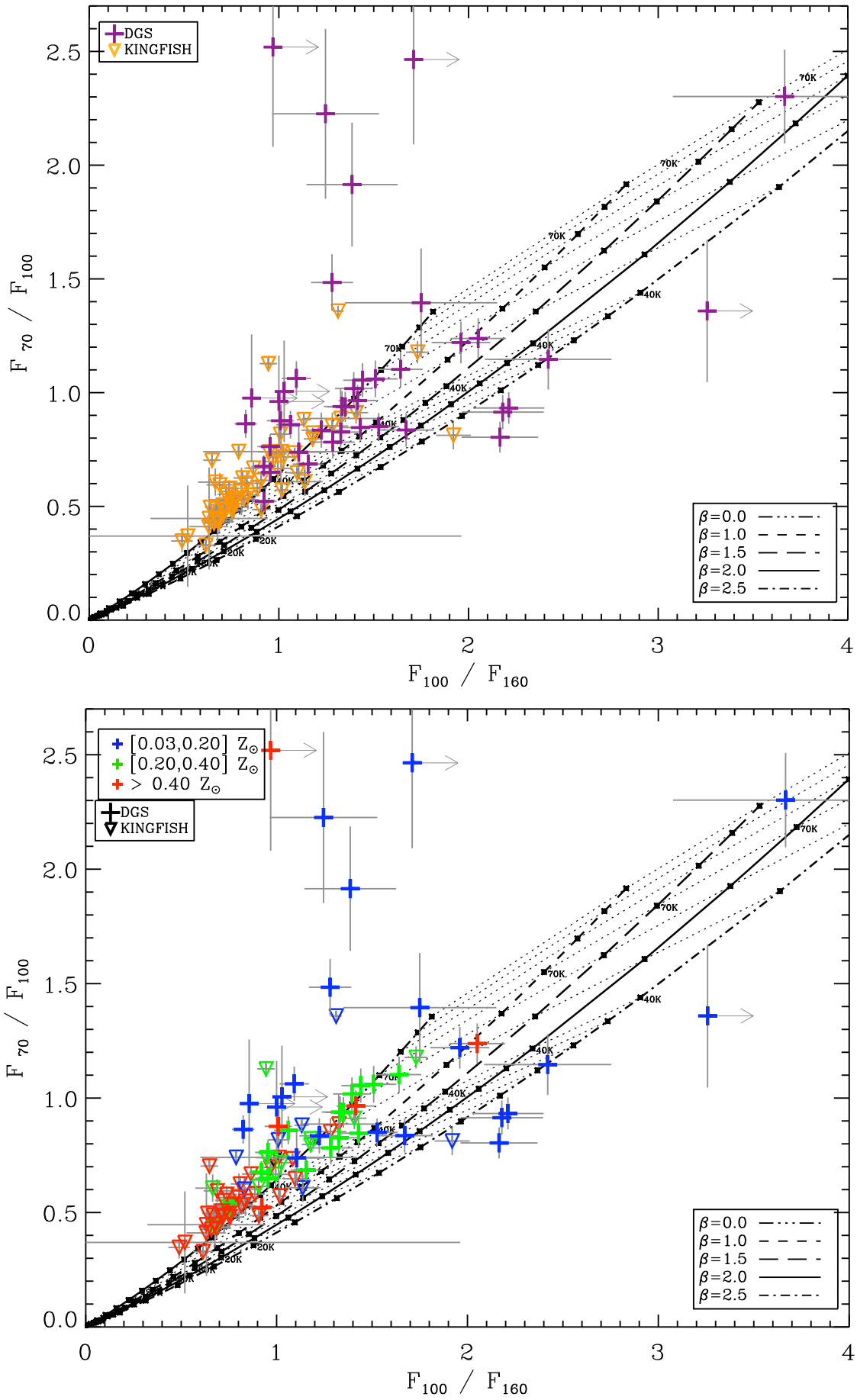

Fig. 9. Colour-colour diagram: PACS/PACS diagram: F_{70}/F_{100} versus F_{100}/F_{160}. *(top)* The colour and symbol code differentiates DGS (purple crosses) and KINGFISH galaxies (orange downward triangles). *(bottom)* The colour code delineates the different metallicity bins this time. Crosses and downward triangles are still representing DGS and KINGFISH galaxies, respectively. For both plots, the curves give theoretical Herschel flux ratios for simulated modified black bodies for β_{theo} = 0.0 to 2.5 and T from 0 to 40 K in 2 K bins and from 40 to 100 K in 10 K bins, as black dots, increasing in T from left to right. Lines of constant T are indicated as dotted lines, and a few temperatures have been marked on the plots.

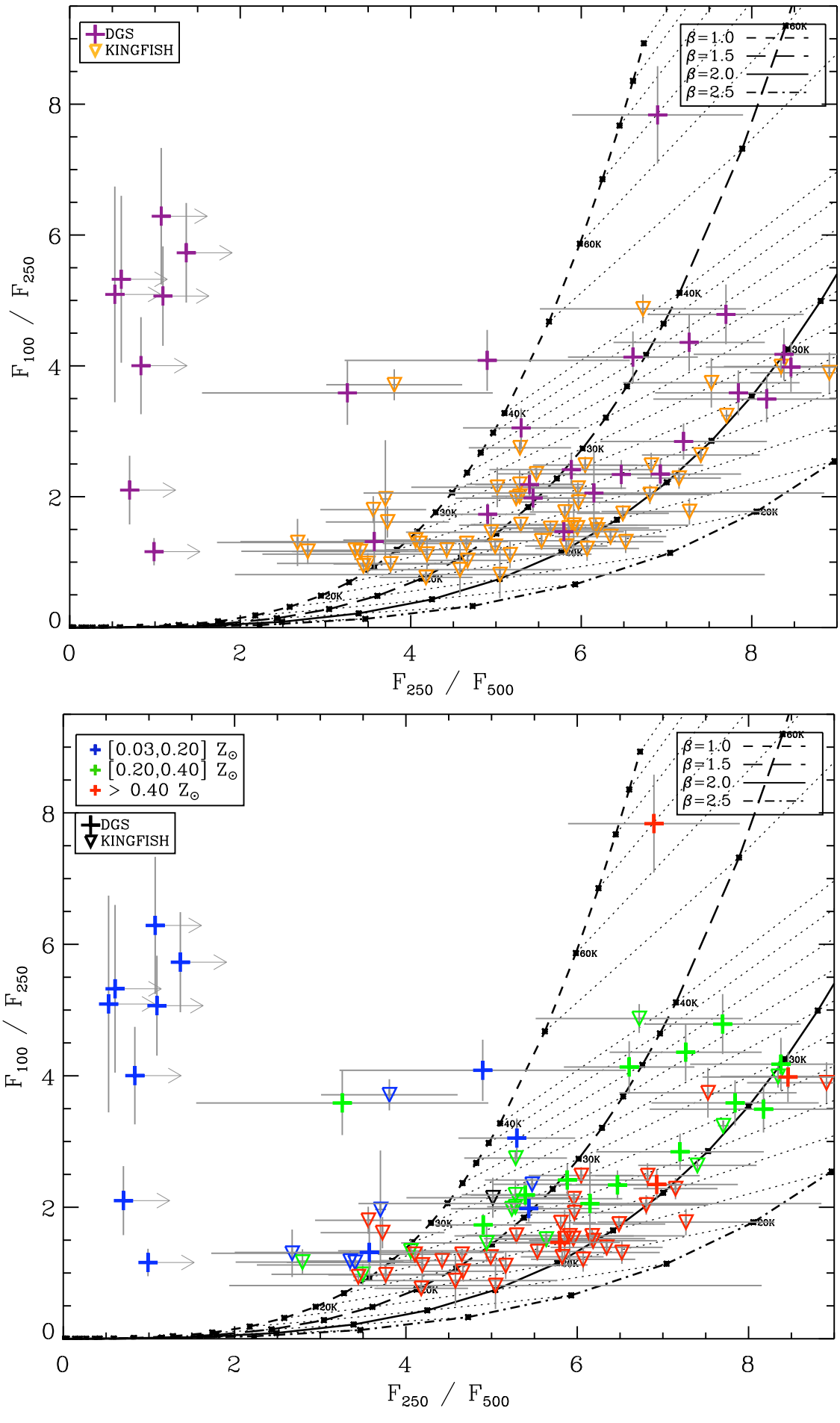

Fig. 10. Colour-colour diagram: PACS/SPIRE diagram: F_{100}/F_{250} versus F_{250}/F_{500}. The colour and symbol choices are the same as in Figure 9 for both figures. Note that the most metal-poor galaxies (from 0.03 to 0.20 $Z_{\odot}$) are very faint and even not detected anymore at long wavelengths. We were only able to derive upper limits beyond 160 μm for these galaxies and, thus, some galaxies do not appear on this diagram anymore.

Table 4. Table of modified blackbody fit parameters for the DGS galaxies.

Source	Temperature (K)	β_{obs}	$M_{dust-BB}$ ($M_\odot$)	L_{FIR-BB} ($L_\odot$)
Haro11	38^{+11}_{-6}	$1.96^{+0.44}_{-0.41}$	$5.0^{+6.5}_{-3.3} \times 10^6$	$5.3^{+1.1}_{-0.5} \times 10^{10}$
Haro2	25^{+3}_{-1}	$2.38^{+0.09}_{-0.38}$	$2.1^{+0.5}_{-0.9} \times 10^6$	$2.5^{+0.1}_{-0.1} \times 10^9$
Haro3	26^{+3}_{-2}	$2.15^{+0.31}_{-0.34}$	$1.7^{+1.1}_{-0.8} \times 10^6$	$2.4^{+0.2}_{-0.1} \times 10^9$
He2-10	26^{+4}_{-1}	$2.24^{+0.21}_{-0.40}$	$1.3^{+0.5}_{-0.7} \times 10^6$	$2.0^{+0.1}_{-0.1} \times 10^9$
HS0017+1055[2a]	98^{+34}_{-36}	$0.00^{+1.34}_{-0.00}$	$1.9^{+8.2}_{-1.4} \times 10^3$	$3.4^{+0.3}_{-0.4} \times 10^8$
HS0052+2536	37^{+14}_{-9}	$1.20^{+0.79}_{-0.73}$	$1.1^{+3.1}_{-0.8} \times 10^6$	$8.5^{+1.6}_{-1.0} \times 10^9$
HS0822+3542	-	-	-	-
HS1222+3741	-	-	-	-
HS1236+3937	-	-	-	-
HS1304+3529[1]	32^{+7}_{-3}	$2.05^{+0.47}_{-0.72}$	$2.2^{+1.5}_{-1.3} \times 10^5$	$9.4^{+0.5}_{-0.4} \times 10^8$
HS1319+3224	-	-	-	-
HS1330+3651[2b]	50^{+3}_{-8}	$0.00^{+0.61}_{-0.00}$	$3.3^{+3.4}_{-0.6} \times 10^4$	$8.8^{+0.4}_{-0.4} \times 10^8$
HS1442+4250	-	-	-	-
HS2352+2733	-	-	-	-
IZw18	-	-	-	-
IC10	21^{+3}_{-1}	$2.25^{+0.26}_{-0.49}$	$2.6^{+1.1}_{-1.4} \times 10^5$	$1.1^{+0.0}_{-0.0} \times 10^8$
IIZw40	33^{+5}_{-4}	$1.71^{+0.41}_{-0.32}$	$1.9^{+1.8}_{-0.9} \times 10^5$	$9.2^{+0.9}_{-0.7} \times 10^8$
Mrk1089	23^{+1}_{-1}	$2.34^{+0.15}_{-0.39}$	$2.5^{+0.7}_{-1.2} \times 10^7$	$1.6^{+0.1}_{-0.1} \times 10^{10}$
Mrk1450	43^{+40}_{-13}	$1.35^{+1.00}_{-0.92}$	$7.6^{+24.6}_{-6.1} \times 10^3$	$1.2^{+0.4}_{-0.2} \times 10^8$
Mrk153[1]	32^{+5}_{-2}	$2.33^{+0.15}_{-0.61}$	$1.2^{+1.4}_{-0.6} \times 10^5$	$5.3^{+0.3}_{-0.2} \times 10^8$
Mrk209[1]	34^{+6}_{-3}	$1.95^{+0.42}_{-0.47}$	$2.1^{+1.4}_{-1.1} \times 10^3$	$1.3^{+0.1}_{-0.1} \times 10^7$
Mrk930	26^{+4}_{-2}	$2.22^{+0.21}_{-0.43}$	$5.7^{+3.0}_{-3.0} \times 10^6$	$8.6^{+0.6}_{-0.5} \times 10^9$
NGC1140	23^{+2}_{-1}	$2.17^{+0.31}_{-0.36}$	$3.0^{+1.7}_{-1.5} \times 10^6$	$1.9^{+0.1}_{-0.1} \times 10^9$
NGC1569	28^{+4}_{-2}	$2.20^{+0.28}_{-0.38}$	$2.8^{+1.5}_{-1.4} \times 10^5$	$5.7^{+0.5}_{-0.4} \times 10^8$
NGC1705	33^{+5}_{-4}	$1.16^{+0.33}_{-0.28}$	$8.4^{+6.7}_{-3.7} \times 10^3$	$4.1^{+0.3}_{-0.3} \times 10^7$
NGC2366	39^{+4}_{-4}	$0.96^{+0.22}_{-0.23}$	$6.8^{+2.9}_{-2.1} \times 10^3$	$7.3^{+0.3}_{-0.2} \times 10^7$
NGC4214	26^{+3}_{-3}	$1.39^{+0.37}_{-0.37}$	$2.0^{+2.0}_{-1.0} \times 10^5$	$2.9^{+0.2}_{-0.1} \times 10^8$
NGC4449	22^{+3}_{-1}	$2.18^{+0.27}_{-0.41}$	$2.3^{+1.2}_{-1.2} \times 10^6$	$1.4^{+0.1}_{-0.1} \times 10^9$
NGC4861	28^{+3}_{-3}	$1.36^{+0.34}_{-0.32}$	$6.1^{+5.2}_{-2.7} \times 10^4$	$1.3^{+0.1}_{-0.1} \times 10^8$
NGC5253	30^{+5}_{-3}	$1.86^{+0.40}_{-0.37}$	$1.9^{+1.8}_{-1.0} \times 10^5$	$5.5^{+0.5}_{-0.4} \times 10^8$
NGC625	29^{+4}_{-3}	$1.33^{+0.35}_{-0.30}$	$5.9^{+5.9}_{-2.7} \times 10^4$	$1.5^{+0.1}_{-0.1} \times 10^8$
NGC6822	26^{+4}_{-4}	$0.99^{+0.59}_{-0.50}$	$1.1^{+1.6}_{-0.6} \times 10^4$	$1.8^{+0.1}_{-0.1} \times 10^7$
Pox186	40^{+4}_{-4}	$0.00^{+0.00}_{-0.00}$	$1.6^{+0.7}_{-0.5} \times 10^3$	$2.0^{+0.2}_{-0.2} \times 10^7$
SBS0335-052[2a,3]	89^{+10}_{-8}	$1.64^{+0.39}_{-0.33}$	$8.0^{+1.8}_{-1.4} \times 10^2$	$1.2^{+1.4}_{-1.2} \times 10^7$
SBS1159+545	-	-	-	-
SBS1211+540[2a,3]	71^{+7}_{-7}	$0.34^{+0.46}_{-0.41}$	$1.0^{+0.4}_{-0.3} \times 10^2$	$1.2^{+0.1}_{-0.1} \times 10^7$
SBS1249+493	-	-	-	-
SBS1415+437[2b]	35^{+16}_{-3}	$2.37^{+0.15}_{-1.20}$	$4.9^{+2.1}_{-3.1} \times 10^3$	$3.5^{+0.3}_{-0.3} \times 10^7$
SBS1533+574[2a]	42^{+8}_{-10}	$0.44^{+1.00}_{-0.40}$	$5.6^{+11.4}_{-2.5} \times 10^4$	$8.2^{+0.4}_{-0.4} \times 10^8$
Tol0618-402	-	-	-	-
Tol1214-277	-	-	-	-
UGC4483	-	-	-	-
UGCA20	-	-	-	-
UM133	41^{+16}_{-15}	$0.44^{+1.89}_{-0.57}$	$3.1^{+56.4}_{-2.8} \times 10^3$	$4.0^{+0.9}_{-0.5} \times 10^7$
UM311	24^{+3}_{-2}	$1.58^{+0.34}_{-0.39}$	$3.7^{+3.5}_{-1.9} \times 10^6$	$3.4^{+0.2}_{-0.1} \times 10^9$
UM448[1]	33^{+2}_{-2}	$1.99^{+0.18}_{-0.16}$	$9.9^{+3.5}_{-2.5} \times 10^6$	$4.9^{+0.2}_{-0.2} \times 10^{10}$
UM461	24^{+1}_{-1}	$2.50^{+0.00}_{-0.00}$	$2.7^{+0.5}_{-0.5} \times 10^4$	$2.5^{+0.2}_{-0.2} \times 10^7$
VIIZw403[1]	34^{+3}_{-3}	$1.57^{+0.27}_{-0.23}$	$2.1^{+1.1}_{-0.7} \times 10^3$	$1.2^{+0.1}_{-0.0} \times 10^7$

[1]: 70 μm point included in fit: violation of the upper limit condition at 70 μm.
[2a]: 70 μm point included in fit: no detections beyond 160 μm.
[2b]: 70 μm point included in fit: no observations beyond 160 μm.
[3]: For these particular galaxies, we included the 24 μm point in the fit as the 24 μm point fell below the modelled modified blackbody when we just overlaid it on the plot.

4.2.2. Rigorous error estimation

In order to derive conservative errors for our T, β, M_{dust} and L_{FIR} parameters we performed Monte Carlo iterations for each fit, following the method in Galliano et al. (2011). For each galaxy, we randomly perturb our fluxes within the errors bars and perform fits of the perturbed SEDs (300 for each galaxy). To be able to do this we must first carefully identify the various types of error and take special care for errors which are correlated between different bands.

As explained in Sections 3.1.2 and 3.2.2, we have measurement errors and calibration errors in our error estimates. The measurement errors are independent from one band to another and are usually well represented by a Gaussian distribution. The calibration errors, however, are correlated between different bands as it is the error on the flux conversion factor. It can be summarized for our case as follow :

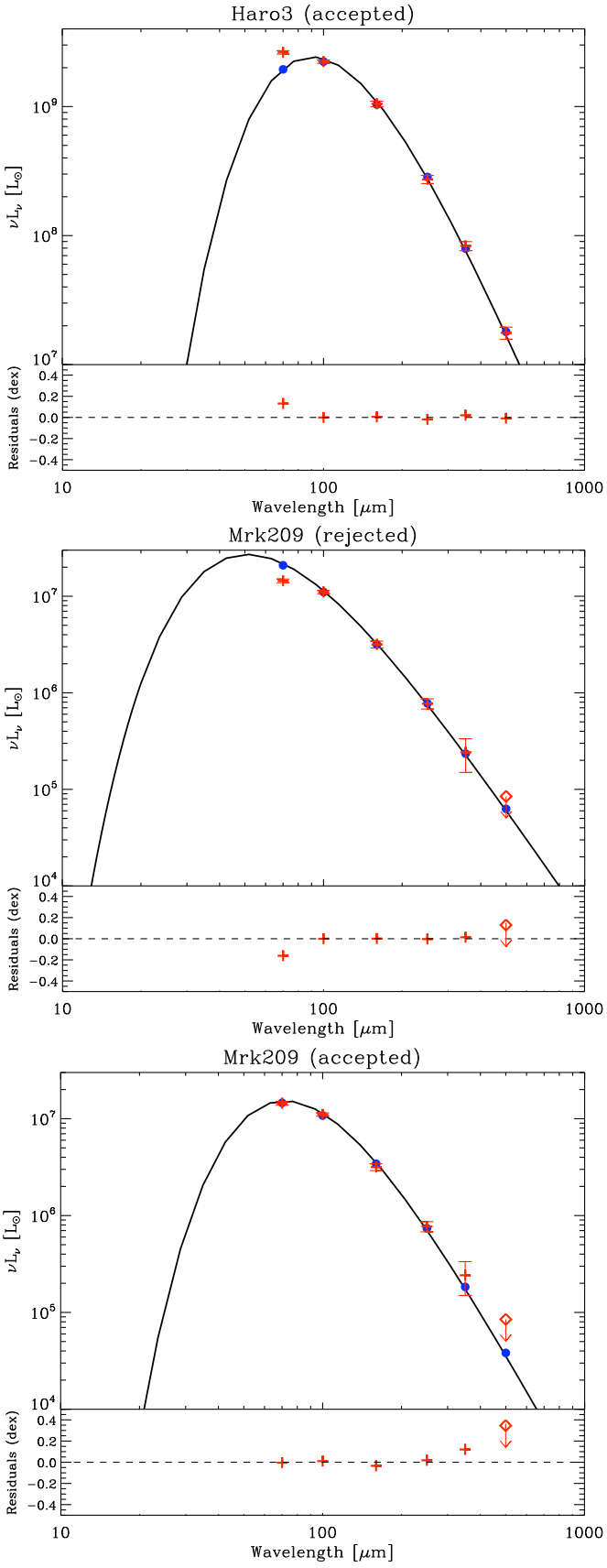

Fig. 11. Examples of modified blackbody fits: the observed points are the red crosses whereas the modelled points are the filled blue circles. Upper limits are indicated with red diamonds. The bottom panel of each plot indicates the residuals from the fit. (*top*) Fit for Haro3, the observed 70 μm point which is not considered at first in our fitting procedure, is above the modelled one. (*centre*) Fit for Mrk209. Here the observed 70 μm point is below the modelled one, and the fit should be redone, giving us: (*bottom*) Fit for Mrk209 using the 70 μm point. Note how the shape of the modified blackbody varies between the two: for example, the dust temperature for Mrk209 goes from 56 K (without 70 μm) to 33K (with 70 μm).

PACS: Although the total calibration error is 5% in the three PACS bands it can be decomposed into two components :

- the uncertainty on the calibration model is 5% (according to the PACS photometre point-source flux calibration documentation[14]) and is correlated between the three bands.
- the uncertainties due to noise in the calibration observations are: 1.4, 1.6, 3.5 % at 70, 100, 160 μm, respectively (PACS photometre point-source flux calibration). These uncertainties are independent from one band to another.

SPIRE: The SPIRE ICC recommend using 7% in each band but here again we can decompose it :

- the uncertainty on the calibration model is 5% (SPIRE Observer's Manual) and is correlated between the three bands.
- the uncertainties due to noise in the calibration observations are 2% for each band (SPIRE Observer's Manual). These uncertainties are independent.
- As SPIRE maps are given in Jy·beam^{-1}, the error on the beam area will also affect the calibration. The uncertainty on the beam area is given to be 4% in each band[15] and is independent.

The perturbation of the observed fluxes will then be the sum of two components :

- A normal random independent variable representing the measurement errors.
- A normal random variable describing the calibration errors that takes into account the correlation between the wavebands as described above, the same for each galaxy.

After performing 300 Monte-Carlo iterations, a distribution for each of the three model parameters T, β, M_{dust} as well as for L_{FIR} is obtained for each galaxy (see example on Fig. 12). We chose to quote the 66.67% confidence level for our parameters defined by the range of the parameter values between 0.1667 and 0.8333 of the repartition function. As the distributions are often asymmetric we obtain asymmetric error bars on our parameters. These error bars are given in Table 4.

4.2.3. FIR properties

We now have the T, β, M_{dust} and L_{FIR} distributions of the DGS. We perform the same analysis for the KINGFISH sample in order to compare the distribution of parameters of the dwarf galaxies with those of the KINGFISH sample (Figures 13 and 14). Note that KINGFISH is not a volume- or flux-limited sample but a cross-section of galaxies with different properties. Due to the heterogeneity of both samples we thus quote the median rather than the mean to compare the samples.

Temperature

The range in dust temperature of the DGS galaxies is 21 to 98 K with a median $T \sim 32$ K (Figure 13a). The most metal-poor galaxies are among the warmer ones. If we compare the KINGFISH to the DGS galaxies, our lowest temperatures are quite comparable (17 vs 21 K), but the DGS galaxies have

[14] http://herschel.esac.esa.int/twiki/bin/view/Public/PacsCalibrationWeb?template=viewprint

[15] This value is given in: http://herschel.esac.esa.int/twiki/bin/view/Public/SpirePhotometerBeamProfileAnalysis.

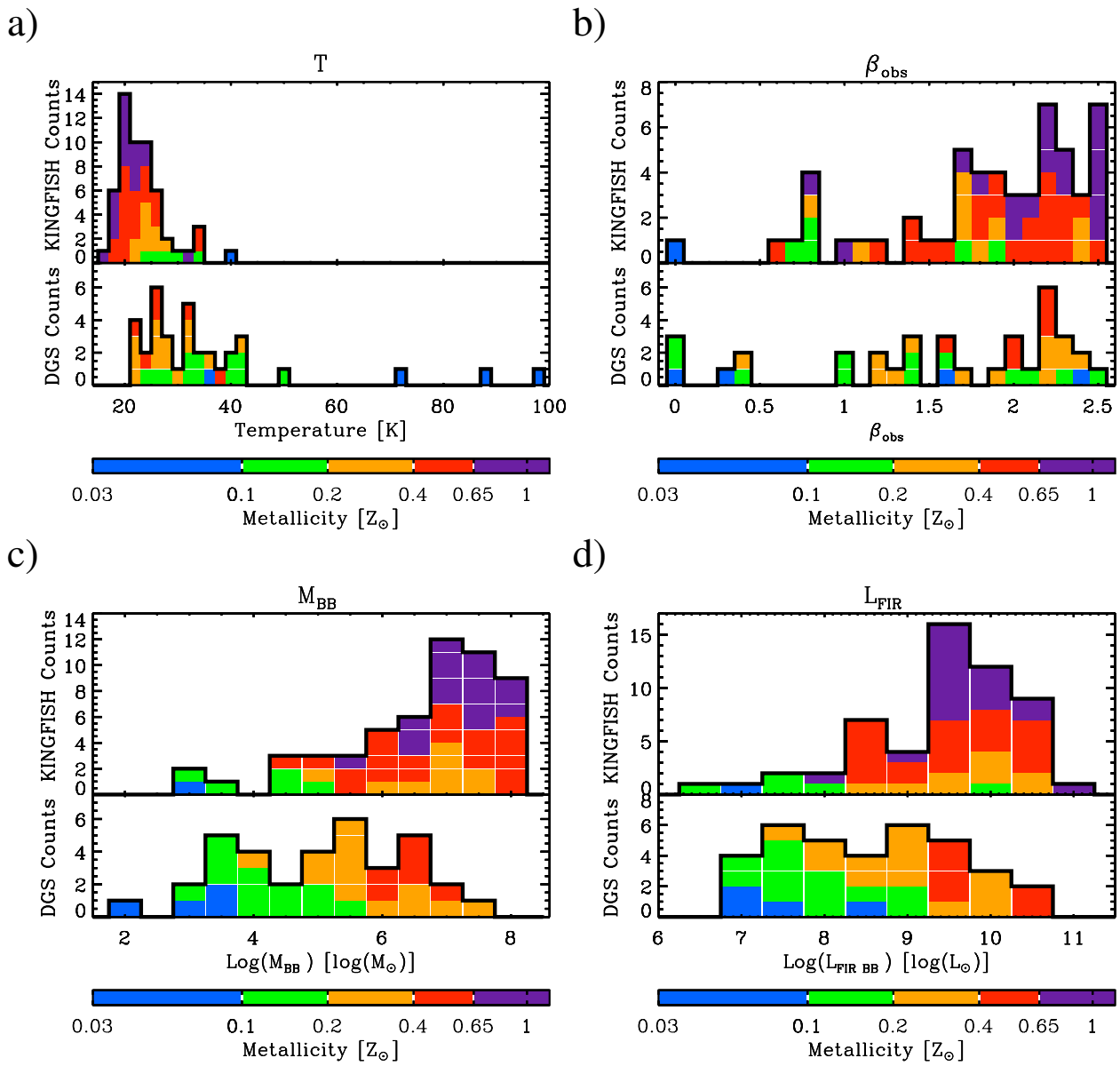

Fig. 13. Distributions of temperature *(a)*, emissivity index *(b)*, dust mass *(c)* and FIR luminosity *(d)* from modified blackbody fits for *Herschel* data for the DGS and KINGFISH samples. The colour scale represents the range of metallicity values. On each panel, the upper/lower histogram is the KINGFISH/DGS distribution for the parameter.

higher maximal dust temperatures (39 vs 98 K). In Figure 13a, we see that the KINGFISH dust temperature distribution has a narrow peak around ~20-25 K whereas the DGS distribution is broader. This difference is due to some galaxies in our sample that peak at extremely short wavelengths, a distinguishing feature of star-forming dwarf galaxies, resulting in very high dust temperatures for a single modified blackbody fit. The dust in DGS galaxies is thus overally warmer than that in more metal-rich galaxies (T^{med}_{DGS} = 32 K and $T^{med}_{KINGFISH}$ = 23 K). This is coherent with the temperature trends presented in the previous section. Note that the high temperature tail of the DGS temperature distribution could be even more prominent: some galaxies are not detected beyond 100-160 μm rendering impossible the determination of their dust temperature with a modified blackbody fit (13 galaxies in the DGS). The SEDs for these galaxies likely peak at very short wavelengths giving very warm average dust temperatures.

Emissivity index

The "observed" emissivity index (β_{obs}, see Eq. 10) distribution is shown on Figure 13b, spanning a range from 0.0 to 2.5 with a median $\beta_{obs} \sim 1.7$. There does not appear to be any clear correlation with metallicity here. Nonetheless, even if some DGS galaxies are nicely fitted by an often-presumed $\beta_{obs} = 2.0$ blackbody, some require a $\beta_{obs} \leq 2.0$, and those are primarily metal-poor to moderately metal-poor galaxies (0.10 to 0.4 $Z_\odot$). Note also that for the KINGFISH sample, all of the galaxies, but two, within this metallicity range have $0.5 \leq \beta_{obs} \leq 2.0$. From SPIRE band ratios, Boselli et al. (2012) also found that low-metallicity galaxies from the HRS sample were presenting submm colours consistent with an emissivity index ≤ 2.0. Arbitrarily fixing $\beta = 2.0$ in blackbody fitting, in order to

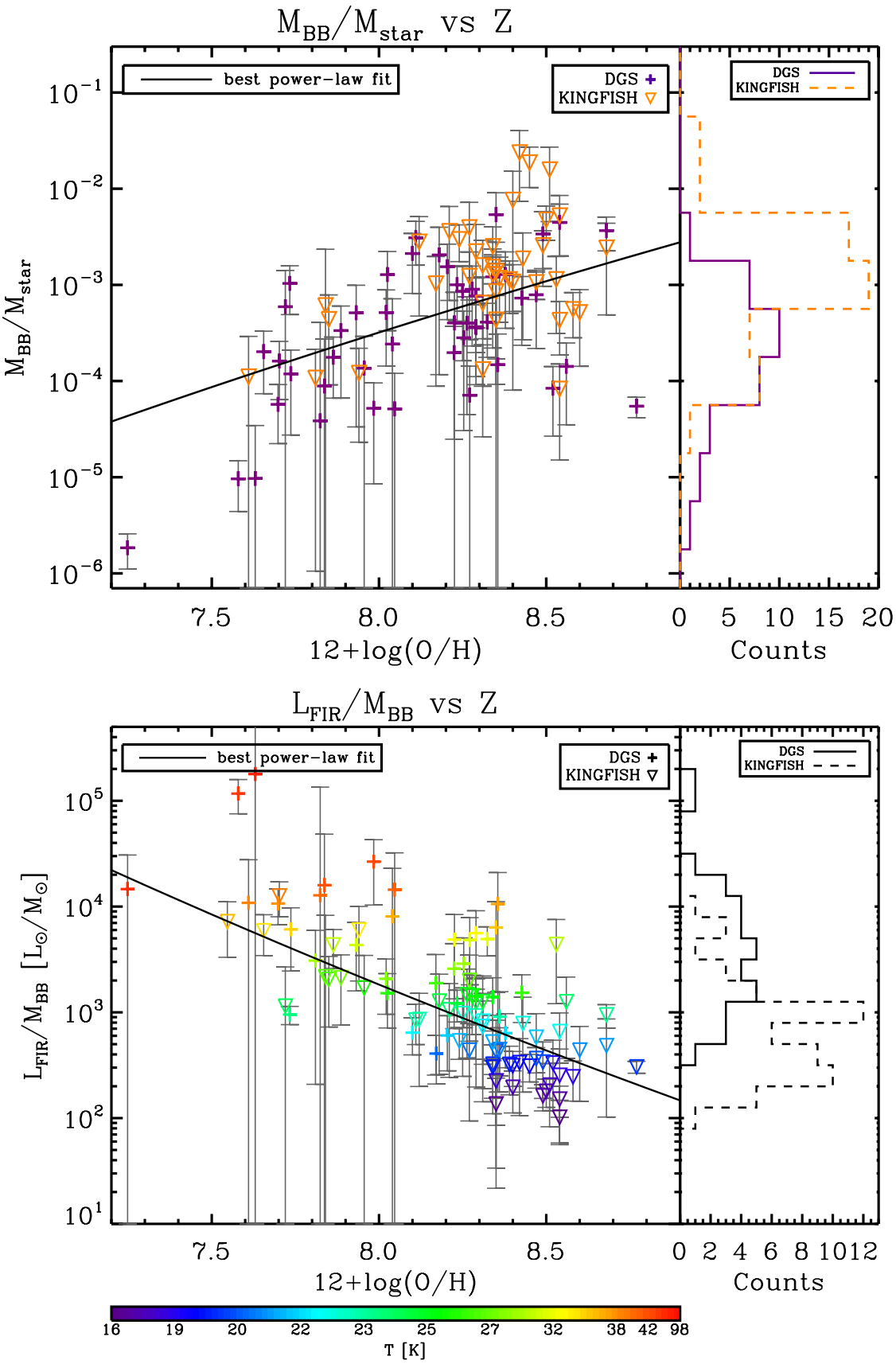

Fig. 14. *(top)* M_{BB}/M_{star} as a function of metallicity for DGS (purple crosses) and KINGFISH (orange downward triangles). The best power-law fit is indicated as a black line, and corresponds to: $\log(M_{BB}/M_{star})$ = (-21.8 ± 1.5) + (20.3 ± 1.6) × log(12+log(O/H)). The distribution of M_{BB}/M_{star} is indicated on the side for both samples: plain purple line for DGS and dashed orange line for KINGFISH. *(bottom)* L_{FIR}/M_{BB} as a function of metallicity for DGS (crosses) and KINGFISH (downward triangles). The colours code the temperature, T. The best power-law fit line is indicated as a black line, and corresponds to: $\log(L_{FIR}/M_{BB})$ = (24.4 ± 1.1) + (-23.6 ± 1.2) × log(12+log(O/H)). The distribution of L_{FIR}/M_{BB} is indicated on the side for both samples: plain line for DGS and dashed line for KINGFISH. On both plots: the errors on the metallicities are omitted for clarity. They are of about 0.1 dex on average.

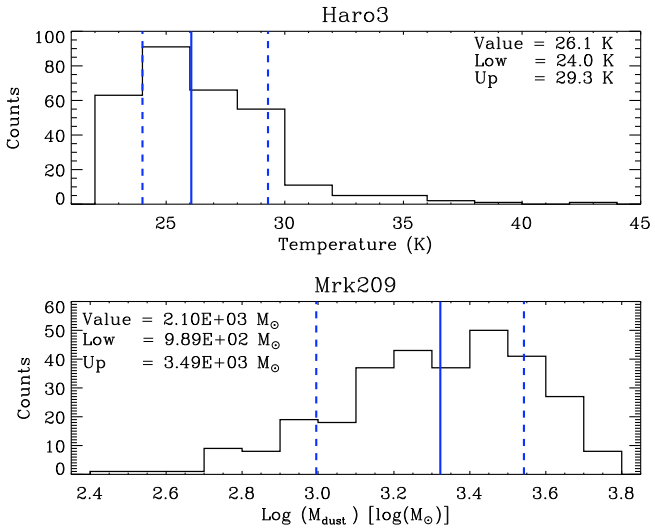

Fig. 12. Examples of the obtained parameter distributions for the 300 Monte-Carlo iterations for the modified blackbody fits: (*top*) distribution of temperature, T, for Haro3, (*bottom*) distribution of dust mass, M_{dust}, for Mrk209 with the 70 μm point included in the fit. The plain blue line notes the value of the parameter and the dashed blue lines note the 66.67% confidence level for the parameters.

mimic the emissivity index appropriate for a mixture of amorphous silicate and graphite (reproducing the Milky Way observations), may not always be appropriate for low-metallicity galaxies. However, we note that several DGS galaxies suggest a β_{obs} = 0.0-0.5. These six galaxies with $\beta_{obs} < 0.5$ in the DGS, are not detected beyond 160 μm and such a low β_{obs} is probably due to the poorly constrained submm part of the SED.

In summary, there are metal-poor to moderately metal-poor galaxies, with metallicities between 0.1 and 0.4 $Z_{\odot}$, for which $0.5 \leq \beta_{obs} \leq 2.0$. These lower β_{obs} values, not necessarily realistic in term of actual grain properties, are representative of a flatter submm slope in the FIR observations, and could perhaps be an indicator of the presence of a submm excess in these sources (see Section 4.3).

Dust mass

The dust masses estimated from our modified blackbody fits range from 1.0×10^2 to 2.5×10^7 $M_{\odot}$ (Figure 13c), with a median of $\sim 1.2 \times 10^5$ $M_{\odot}$. From Figure 13c we see that the most metal-poor galaxies are the least massive galaxies compared to the moderately metal-poor galaxies. The dwarf galaxies are, not surprisingly, less massive in dust than the galaxies from the KINGFISH sample: the median dust mass of the KINGFISH sample is about two orders of magnitude higher than for the DGS: $\sim 1.1 \times 10^7$ $M_{\odot}$. In order to determine if this is only an effect due to the smaller sizes of dwarfs, we consider the ratio between the dust and stellar masses. The stellar masses for KINGFISH can be found in Skibba et al. (2011) and the DGS stellar masses in Madden et al. (2013). Figure 14 shows that there is a strong decrease (two orders of magnitude) of the proportion of dust mass relative to the stellar mass with decreasing metallicity: we have a Spearman rank coefficient[16] ρ=0.58. The median for the ratio M_{BB}/M_{star} is 0.02% for DGS versus 0.1% for KINGFISH. The best power-law fit gives:

$$M_{BB}/M_{star} = 1.6 \times 10^{-22} \times (12 + log(O/H))^{20.3} \quad (11)$$

The stellar masses from the DGS are derived from the formula of Eskew et al. (2012) from the IRAC 3.6 and 4.5 μm broadband flux densities. The scatter in their relation corresponds to a 1σ uncertainties for their stellar masses of $\sim$ 30%, which is within the uncertainties we have for the DGS stellar masses ($\sim$ 50% on average). The stellar masses for KINGFISH have been derived by Skibba et al. (2011) following Zibetti et al. (2009) from optical and NIR colours. With this estimate, the KINGFISH stellar masses could be biased low by up to 40% Zibetti et al. (2009). Even if this could decrease the ratios by a factor of $\sim$ 1.7, this could not explain the order of magnitude difference seen between the dust-to-stellar mass ratios of the two samples.

However the dust masses derived here for both samples are probably lower limits of the real dust masses in many cases (for example, see Dale et al. 2012, for KINGFISH). Indeed we allow our β_{obs} to go to very low values, giving lower dust masses than if we fixed it to 1.5 or even 2.0: as we allow a greater emission effciency for the grains, we need less mass than if we were using a higher emissivity index, to account for the same amount of luminosity. We perform the test by fixing the emissivity index parameter to 1.5 then 2.0 but find that the dust masses were increasing by only a factor $\sim$ 1.5 - 3, again insufficient to explain the order of magnitude difference between the proportion of dust relative to the stars between the metal-poor and metal-rich galaxies. Nonetheless, with our modified blackbody fits we are considering only one temperature and grain size. We may be missing here a fraction of the dust mass coming from warmer big grains, and this contribution may be more important in low-metallicity galaxies rather than in more metal-rich ones. Thus, part of the observed trend may just be a side effect of using modified blackbodies. The mass corresponding to the stochastically heated grains is, however, negligible. In a follow-up paper (Rémy-Ruyer et al. 2013, in prep.), we will obtain total dust masses from a full semi-empirical SED model, which will allow us to study this effect in more details.

FIR luminosity

The FIR luminosities in the DGS sample range from 1.2×10^7 to 5.3×10^{10} $L_{\odot}$ (Figure 13d), with a median of $\sim 5.3 \times 10^8$ $L_{\odot}$. We see in Figure 13d that dwarf galaxies are less luminous in the FIR than the galaxies from the KINGFISH sample. However if we consider L_{FIR}/M_{BB}, which represents the quantity of light emitted by the available amount of dust, there is a strong trend of increasing L_{FIR}/M_{BB} with decreasing metallicity (Figure 14): here we have a Spearman rank coefficient ρ=-0.72. The best power-law fit gives:

$$L_{FIR}/M_{BB} = 4.2 \times 10^{24} \times (12 + log(O/H))^{-23.6} \quad (12)$$

Despite their lower dust masses, dwarf galaxies emit more in the FIR/submm than more metal-rich galaxies, per unit dust mass ($\sim$ six times more for the DGS). Here again, fixing β_{obs}=2 would only change the dust masses by a factor of 1.5 - 3,

[16] The Spearman rank coefficient, ρ, indicates how well the relationship between X and Y can be described by a monotonic function: monotonically increasing: $\rho > 0$, or monotonically decreasing: $\rho < 0$.

insufficient to explain the difference between the two samples. This difference is rather a direct consequence of the higher temperature of dust grains in dwarf galaxies, as shown by the colours on Fig. 14, due to the stronger and harder ISRF in which the grains are embedded. However, as mentioned above, the total dust mass may be underestimated by the modified blackbody model in lower metallicity galaxies and this trend could be weaker.

Temperature - emissivity index relation

Some studies have noted an inverse β / temperature correlation in objects from starless cores to galaxies (Dupac et al. 2003; Yang & Phillips 2007; Anderson et al. 2010; Paradis et al. 2010; Planck Collaboration et al. 2011a; Galametz et al. 2012; Smith et al. 2012a). To investigate this possible effect in the DGS sample, we plot these two parameters from our modified blackbody fits (T and β_{obs}) (Figure 15). We also add the KINGFISH galaxies. First we note that the DGS galaxies have overall higher dust temperature than the KINGFISH galaxies as already noted in Figures 9, 10 and 13. We also have the DGS galaxies where the fit gives β_{obs} = 0.0, without detections beyond 160 μm that we believe to be due to a poorly constrained submm SED. If we exclude these galaxies, the KINGFISH and DGS samples present an anticorrelation between T and β_{obs}, and this anticorrelation seems to be steeper in the DGS: the best power law fit gives $T \propto \beta_{obs}^{-0.48}$ for the DGS and $T \propto \beta_{obs}^{-0.29}$ for the KINGFISH galaxies. However, the anticorrelation seems stronger in KINGFISH than in the DGS sample ($\rho_{KINGFISH}$= -0.69 vs ρ_{DGS}= -0.56).

Shetty et al. (2009a,b) and Juvela & Ysard (2012a,b) showed that such an observed anticorrelation comes from the assumption of a constant temperature along the line-of-sight in modified blackbody fits and from noise in the measurements. They advise caution when interpreting this β / temperature relationship when derived from χ^2 modified blackbody fits. Kelly et al. (2012) show that a χ^2 fit can artificially produce an anticorrelation between T and β_{obs}, where a Bayesian fit does not, and recovers the true parameters more accurately.

Nonetheless, if we assume that the differences in the observed (T, β_{obs}) relations between DGS and KINGFISH can be due to changes in dust optical grain properties in the submm (as suggested in Meny et al. 2007; Paradis et al. 2010), this may be the sign that the assumption of a single grain temperature, the presence of noise in the measurements and the use of a χ^2 fitting procedure may only be *partially* responsible for the observed trends. However, given the very large errors on the T and β parameters, it is difficult to draw a solid conclusion on this issue.

4.3. Submillimetre excess

A submm excess has been observed in the past in several dwarf galaxies (Galliano et al. 2003, 2005; Galametz et al. 2009; Bot et al. 2010; Grossi et al. 2010). It has been called "excess" because the current available models are unable to fully explain the submm emission of these galaxies. In most models, β_{theo} = 2 is often assumed in order to mimic the optical properties of the dust grain mixture of the Galaxy. In spiral galaxies, a modified blackbody with a fixed β_{theo} to 2 reproduces well the FIR emission (Bendo et al. 2003, 2010). In the colour-colour diagrams we hinted that a low β_{obs} may be the sign of a possible presence of an excess emission adding its contribution to a β_{theo} = 2 submm SED. Boselli et al. (2012) also showed that the F_{250}/F_{500} colour was more consistent with an effective emissivity index of 1.5 for the lowest metallicity galaxies in the HRS sample. Here we want to determine, systematically, which galaxies of the DGS and KINGFISH samples present an excess. A modified blackbody with a fixed emissivity index β_{theo} of 2.0 is fit to the data for both DGS and KINGFISH samples (109 galaxies in total). Here again, we use the 70 μm point only if the modelled flux is larger than the observed flux.

We take the relative residual at 500 μm to be:

$$R(500) = \frac{L_\nu^{observed}(500) - L_\nu^{model}(500)}{L_\nu^{model}(500)} \quad (13)$$

In order to define a residual, R, at 500 μm the galaxy must be detected out to 500 μm. This, unfortunately, reduces our sample to 78 galaxies due to the high number of faint galaxies in the DGS sample.

Following the same procedure as in Section 4.2.2, we randomly perturb the fluxes within the errors bars and perform fits of the perturbed SEDs (300 for each galaxy). A distribution of *R(500)* is generated and the 66.67% confidence level of the distribution gives the error on the residual at 500 μm: Δ*R(500)*. The values of *R(500)* and Δ*R(500)* are listed in Table 5.

A galaxy is then flagged with "excess" if the relative residual at 500 μm is greater than the corresponding error: *R(500)* >Δ*R(500)* (see Table 5). As the 500 μm point is included in the fit, the procedure will also try to achieve a good fit of the 500 μm point, and this will give lower *R(500)* than if the 500 μm point was not included in the fit. That is why we fix our "excess" criterion to a 1σ detection only. For both samples, the *R(500)* distribution is shown in Figure 16, and excess galaxies are indicated by hashed cells.

Table 5. Table of relative residuals at 500 μm for a modified blackbody fit with β_{theo} fixed to 2.0 for the DGS sample. A column with the β_{obs} values from Table 4 have been added.

	β_{obs}	β_{theo} **= 2.0**		
Source		*R(500)* (%)	Δ*R(500)* (%)	Excess ?
Haro11	1.96	27.6	10.8	yes
Haro2	2.38	-6.4	13.7	
Haro3	2.15	-2.3	11.8	
He2-10	2.24	-3.3	9.8	
HS0052+2536	1.20	154.2	19.6	yes
IC10	2.25	0.1	26.9	
IIZw40	1.71	2.2	8.0	
Mrk1089	2.34	-3.6	14.2	
Mrk930	2.22	8.3	28.9	
NGC1140	2.17	-3.6	17.3	
NGC1569	2.20	1.4	9.2	
NGC1705	1.16	42.5	17.6	yes
NGC2366	0.96	39.6	12.4	yes
NGC4214	1.39	17.9	8.2	yes
NGC4449	2.18	1.2	8.9	
NGC4861	1.36	32.5	15.7	yes
NGC5253	1.86	8.5	8.5	
NGC625	1.33	21.6	9.4	yes
NGC6822	0.99	96.8	19.7	yes
UM311	1.58	9.4	9.5	
UM448	1.99	6.9	16.2	
VIIZw403	1.57	71.7	23.0	yes

Out of 78 galaxies, 45% present an excess at 500 μm with respect to a β_{theo} = 2 modified blackbody: nine are from DGS and 26 from KINGFISH. It is interesting to note that eight out of

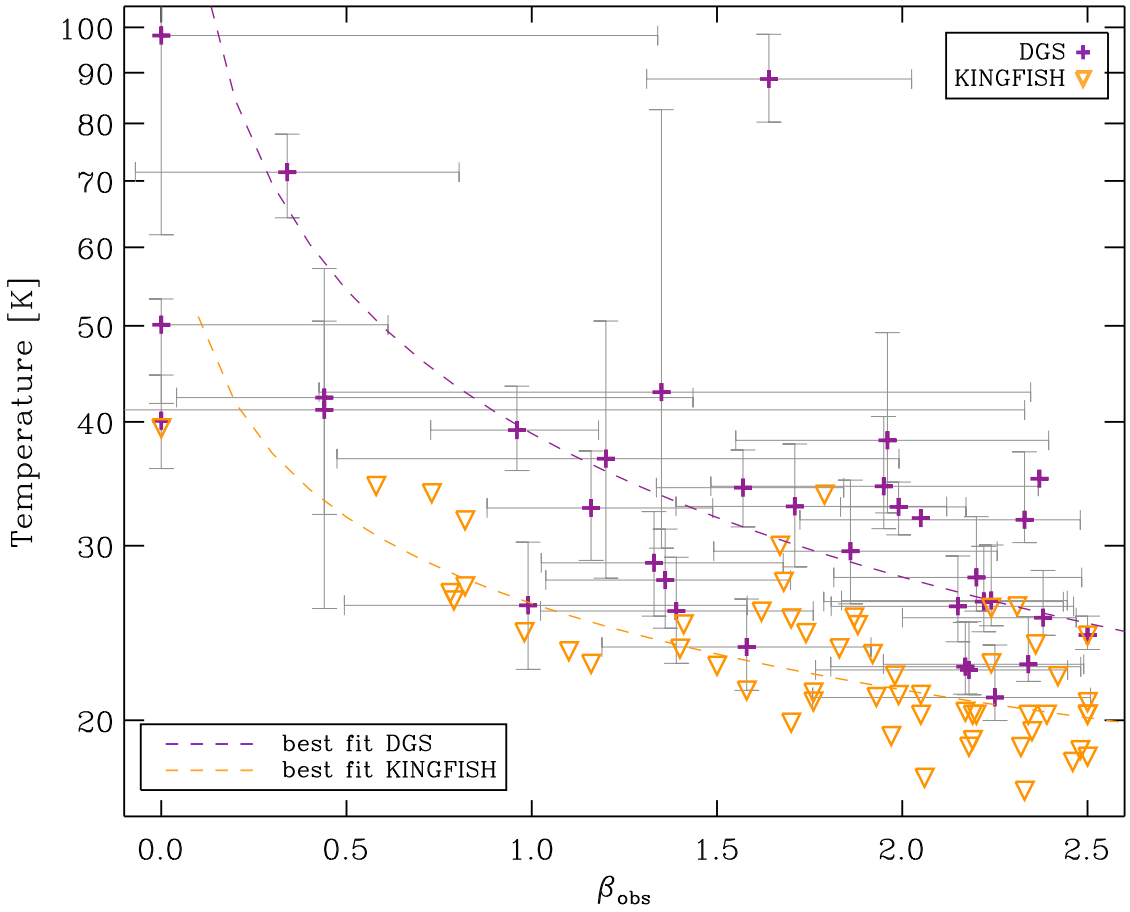

Fig. 15. Temperature versus β_{obs} from the modified blackbody fits for the DGS (purple crosses) and for KINGFISH galaxies (orange downward triangles). The dotted lines correspond to the best power law fit for the DGS (purple) and KINGFISH (orange) galaxies, excluding the galaxies for which β_{obs}=0.0. They correspond to: $\log(T_{DGS})$ = (1.59 ± 0.01) + (-0.48 ± 0.04) × $\log(\beta_{obs,DGS})$, and $\log(T_{KINGFISH})$ = (1.41 ± 0.02) + (-0.29 ± 0.05) × $\log(\beta_{obs,KINGFISH})$. For clarity the error bars on the parameters have been displayed only for the DGS sample.

the nine KINGFISH galaxies of Irregular type (Im, I0 or Sm) detected at 500 μm, are among the 26 "excess" KINGFISH galaxies. The one missing is HoII which has a very large error bar on the 500 μm flux and thus a very wide *R(500)* distribution. Dale et al. (2012) looked at the residual at 500 μm for a Draine & Li (2007) model fit (see Dale et al. 2012, for details) and also found that most of these Irregular galaxies presented an excess at 500 μm. They mention a dozen KINGFISH galaxies with a *R(500)* above 60%. However as their study is based on a different model than ours, we will not go deeper into any further comparison.

Figure 17 shows the metallicity distribution of the 35 excess galaxies (black line) together with the joint metallicity distribution of DGS and KINGFISH samples (grey line). Note how the absence of detections at 500 μm reduces the low-metallicity tail of the joint metallicity distribution. The metallicity distribution for the excess galaxies peaks around 12+log(O/H) ~ 8.3 and is skewed towards the low-metallicity end of the distribution : 63 % of the excess galaxies are galaxies with $Z < 0.4\ Z_{\odot}$, whereas, in the total distribution of galaxies detected at 500 μm, (grey line on Fig. 17), only 49% of the total number of galaxies are galaxies with $Z < 0.4\ Z_{\odot}$. Moreover, the proportion of excess galaxies in the [7.5 - 8.3] metallicity range is ~ 53% versus ~ 28% in the]8.3 - 8.8] range. This shows that the submm excess seems to occur mainly in metal-poor galaxies, at least when a β_{theo} = 2 modified blackbody model is used. The colours on Fig. 17 code the signal-to-noise ratio of the residual at 500 μm for the excess galaxies. There seems to be a dichotomy in the distribution around 12+log(O/H) ~ 8.3, with the strongest excesses being detected in the lowest metallicity galaxies.

On Fig. 18, we have a clear anti-correlation between *R(500)* and β_{obs} from the modified blackbody fits from Section 4.2.3: ρ=-0.78. For galaxies with a "naturally" flatter slope (i.e. a low β_{obs}), forcing a steeper slope (i.e. fixing β_{theo} = 2.0) will naturally increase the residuals at the longest wavelengths, thus generating the correlation between *R(500)* and β_{obs}.

All of the galaxies showing an excess (i.e. *R(500)* > Δ*R(500)*) have indeed a low β_{obs} ($\beta_{obs} \leq 2.0$) (Fig. 18). It is also interesting to note that this corresponds to 80% of the 44 galaxies with $\beta_{obs} \leq 2.0$. On the colour-colour diagram of Fig. 10, all of the excess galaxies fall on the left side of the β_{theo} = 2.0 line. Moreover, all of the galaxies falling on the left side of the β_{theo} = 1.5 line, except one, present an excess. This is coherent with what is observed on Fig. 18, and can be useful to select potential targets for FIR/submm follow-up observations.

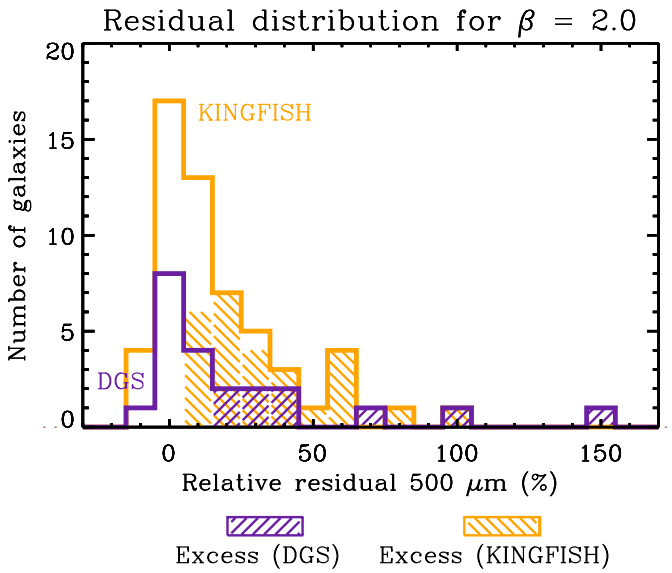

Fig. 16. Relative residual distribution at 500 μm for modified blackbody fits with a fixed β_{theo} of 2.0 for DGS (purple) and KINGFISH (orange) samples. Galaxies for which the residual at 500 μm is greater than the corresponding error bar ($R(500) > \Delta R(500)$) have been marked by hashed cells.

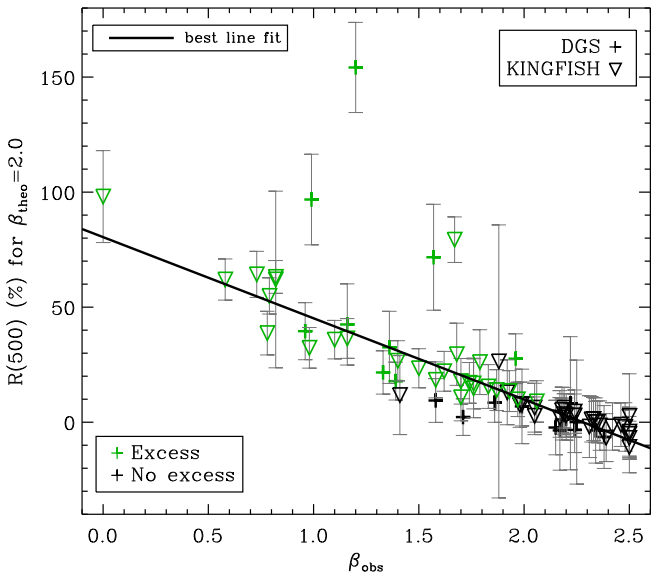

Fig. 18. Relative residual at 500 μm versus β_{obs} (from Section 4.2.3) for DGS (crosses) and KINGFISH (downward triangles) galaxies. The green symbols mark the galaxies presenting an excess at 500 μm. The best fit line is indicated as a solid black line, and corresponds to: R(500)= (80.4 ± 4.1) + (-35.3 ± 2.2) × β_{obs}.

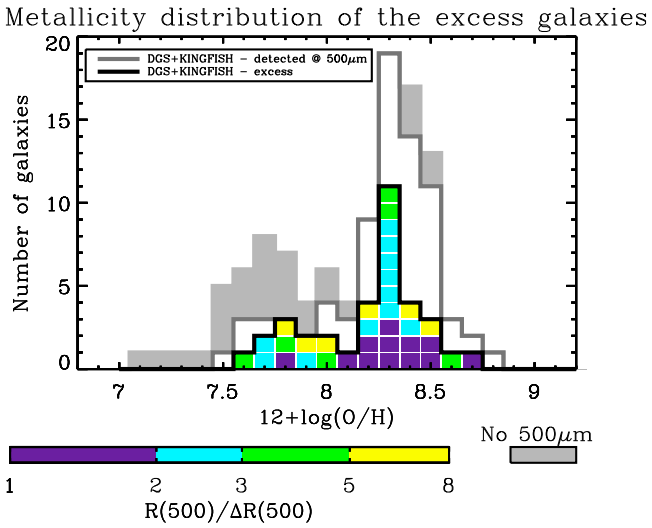

Fig. 17. Metallicity distribution for the excess galaxies in black. The colours mark the presence of an excess at 500 μm and code the intensity of this excess: $R(500)/\Delta R(500)$. The metallicity distribution for the DGS & KINGFISH galaxies detected at 500 μm is outlined in grey. The grey cells mark all of the galaxies for which no detection is available at 500 μm.

4.4. A word of caution: submm excess appearing beyond 500 μm

The previous analysis offers some tools to detect a submm excess in a galaxy. However as we are considering only *Herschel* wavelengths, any galaxy for which a submm excess is appearing beyond *Herschel* wavelengths would not be detected here. This is illustrated with two galaxies of the DGS sample with observations beyond 500 μm, Haro 11 and II Zw 40, both modelled with modified blackbodies, with the same procedure as in Section 4.3. Haro 11 falls to the left side of the $\beta = 1.5$ line and has been identified as an "excess" galaxy in Table 5 whereas II Zw 40 falls to the right side of the $\beta = 1.5$ line (Figure 10) and does not present any excess at 500 μm when using only *Herschel* bands (Table 5).

As shown in Figure 19, Haro 11 presents an excess at 500 μm ($R(500) \sim 28\% \pm 13\%$), confirmed at 870 μm ($R(870) \sim 360\% \pm 15\%$). However the submm excess is clearly appearing at longer wavelengths ($\geq$ 500 μm) for II Zw 40 when including observations beyond 500 μm. At 500 μm $R(500) \sim 2 \pm 8$ %, and $R(450) \sim 6 \pm 34$ % but at 850 and 1200 μm we have $R(850) \sim 265 \pm 16$ % and $R(1200) \sim 370 \pm 40$ %. This illustrates the need for submm data, to complement the existing *Herschel* data. For several galaxies of our sample, new submm observations at 870 μm with LABOCA will soon be available.

This submm excess has been one of the main sources of uncertainty in dust modelling in dwarf galaxies for the past few years, especially on the dust mass parameter. Here we show that this excess does not seem that uncommon even in moderately metal-poor environments and thus understanding its origin is crucial to get accurate dust parameters. Several explanations have already been proposed to investigate the origin of this excess, although not completely satisfactory.

Galliano et al. (2003, 2005), Galametz et al. (2009, 2010, 2011) modelled the submm excess they detected in their metal-poor galaxies with a very cold dust (VCD) component. They added to their SED models an extra modified blackbody with a submm emissivity index of 1 and a low dust temperature (~ 10K). Their additional component could explain the break observed in the submm domain in some of their SEDs but it led to very low gas-to-dust mass ratios, considering the observed gas mass, compared to that expected from chemical evolution and from the amount of available metals in the ISM.

Several studies have shown that fast rotating very small dust grains from ionized gas regions in many galaxies were producing centimetre (cm) radio emission (Ferrara & Dettmar 1994;

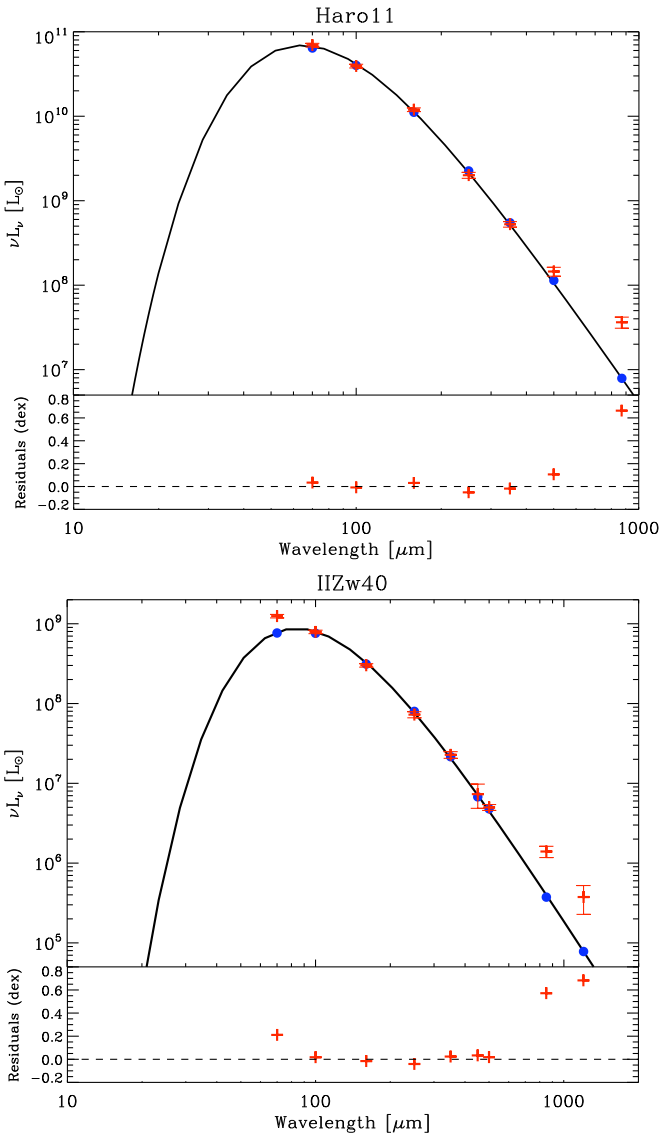

Fig. 19. SEDs of Haro 11 *(top)* and II Zw 40 *(bottom)*. They have been obtained with a modified blackbody model with a fixed β_{theo} = 2.0. The 870 μm point for Haro 11 is from LABOCA (Galametz et al. 2009). For II Zw 40, the 450 and 850 μm points are from SCUBA, and the 1.2 mm point is from MAMBO (Galliano et al. 2005). All submm points have been corrected for non-dust contamination (free-free and synchrotron radiations and CO line contamination). The filled blue circles are the modelled fluxes in each band. The red crosses are the observations. The total SEDs are displayed in black. The bottom panel of each plot indicates the residuals from the fit.

Draine & Hensley 2012). As shown by recent studies (Ysard & Verstraete 2010; Ysard et al. 2012), the peak of the "spinning" dust emission depends on many parameters such as the radiation field intensity, the dust size distribution, dipole moment distribution, physical parameters of the gas phase, etc. This hypothesis was tested to explain the submm/cm excess by Bot et al. (2010), Israel et al. (2010) and Planck Collaboration et al. (2011b) in the Large and Small Magellanic Clouds. The spinning dust model seemed sufficient for the mm/cm excess but another effect is required to explain the submm/mm excess. Indeed, the usual spinning dust models do not normally produce much emission in the submm domain but rather at longer wavelengths (as illustrated in Murphy et al. (2010) for NGC 6946). Moreover, PAHs have been assumed to be the carriers of this spinning dust emission (as shown in Draine & Lazarian 1998) and this may seem contradictory with the weakness of the PAH features observed in low-metallicity galaxies (Engelbracht et al. 2005).

Paradis et al. (2009) showed that the FIR-submm excess in dense molecular clouds of the Galaxy could be explained by fractal aggregation of amorphous individual grains which induces changes in the dust optical properties in the submm. This grain coagulation effect had already been suggested in the past by Bazell & Dwek (1990) and Stepnik et al. (2001).

Meny et al. (2007) proposed a new model for FIR/submm dust emission based on the physical properties of disordered matter. They consider the interaction of electromagnetic waves with the acoustic oscillations in a disordered charge distribution (DCD) and a distribution of low energy two level tunnelling states (TLS). This interaction results in an emission spectrum strongly dependent on the temperature and in an enhanced submm/mm emission compared to more classical models. The emissivity index is no longer constant over this wavelength range. This model has been successfully applied by Bot et al. (2010) to explain the mm excess in the Large Magellanic Cloud (LMC). However, when applied to the Small Magellanic Cloud (SMC), DCD/TLS effects alone do not reproduce the excess well (Bot et al. 2010).

A recent work by Draine & Hensley (2012) on the SMC focuses on magnetic grains as a possible source of submm excess. They consider nanoparticles of metallic iron, magnetite and maghemite that could be free fliers in the ISM or inclusions on larger dust grains. Magnetic grains indeed have an enhanced absorption cross section at submm wavelengths and part of the submm excess could be due to thermal emission from magnetic grain material. They show that a combination of a normal dust mixture (amorphous silicates and carbonaceous grains), spinning dust and magnetic dust could account for the observed SED in the submm/mm range of the SMC.

The various explanations for the submm excess presented here will be explored for the DGS galaxies for which we have submm data, in further studies.

5. Conclusions

We present here the new *Herschel* photometry data for the Dwarf Galaxy Survey, dedicated to the study of the gas and dust properties in the ISMs of 48 low-metallicity galaxies. We perform the data reduction by adapting the map making procedures for extended vs compact sources. We derive flux densities from aperture photometry or from a timeline fitting procedure (for SPIRE point sources) and present here a catalogue of flux densities for the whole sample. We compare our PACS flux densities with corresponding MIPS flux densities to assess their reliability and we found that the MIPS and PACS flux densities are compatible.

We present a first analysis of the FIR/submm behaviour of the DGS galaxies, with modified blackbody fits and several *Herschel* colour-colour diagrams, especially focusing on the comparison with more metal-rich galaxies from the KINGFISH sample, making a total of 109 galaxies, and on the appearance of the submm excess among the samples. We note that:

– Dwarf galaxies present different dust properties than more metal-rich galaxies as in the KINGFISH sample and this can be quantified with modified blackbody fits, to get at the dust

temperatures, emissivity indices, dust masses and FIR luminosities. The differences in the spread of KINGFISH and DGS galaxies on *Herschel* colour-colour diagrams qualitatively reflect these differences in the FIR dust properties and SED shape.

- For modified blackbody fits, the range in dust temperature is 22-98 K and the median dust temperature of the DGS sample is ∼ 32 K. This is warmer than what is observed in more metal-rich galaxies ($T_{KINGFISH}$ ∼ 23 K), and we see a trend of increasing dust temperature with decreasing metallicity. SEDs of lower metallicity galaxies peak at very short wavelengths, often between 50 and 100 μm, and present overall warmer dust.
- Dwarf galaxies show a lower proportion of dust mass relative to stellar mass compared to more metal-rich galaxies (the median for the ratio M_{BB}/M_{star} is 0.02% for DGS versus 0.1% for KINGFISH). Despite their relatively lower dust masses, dwarf galaxies emit more in the FIR/submm than more metal-rich galaxies, per unit dust mass (about six times more for the DGS), reflecting the impact of the very energetic radiation environment on dust grains in dwarfs.
- The range in β_{obs} is 0.0-2.5 for the DGS and KINGFISH samples, with a median of ∼1.7 for the DGS and ∼1.9 for KINGFISH, lower than what is usually taken in SED models ($\beta_{theo} = 2.0$). No clear trend between β_{obs} and metallicity has been noted here. However galaxies with $1.0 \leq \beta_{obs} \leq 2.0$ seem to be primarily metal-poor and moderately metal-poor galaxies ($0.1\ Z_{\odot} < Z < 0.4\ Z_{\odot}$).
- 45% of the DGS and KINGFISH galaxies harbour an excess at 500 μm from a modified blackbody model with $\beta_{theo} = 2.0$, when considering galaxies with detections at 500 μm. This excess seems to appear mainly in lower metallicity galaxies ($Z < 0.4\ Z_{\odot}$), and the strongest excesses are detected in the most metal-poor galaxies. However the submm excess can sometimes only become apparent at wavelengths beyond *Herschel* bands, highlighting the need for submm data beyond 500 μm.

A following paper (Rémy-Ruyer et al. 2013, in prep.) will present the systematic full dust modelling of all of the DGS galaxies with a semi-empirical model which allows for a more realistic description of the dust, and explore in detail the various dust properties of dwarf galaxies. The large ancillary data set, covering the whole IR-to-submm range, will be crucial when performing this multi-wavelength study of the DGS galaxies.

Acknowledgements. The authors would like to thank the referee, Simone Bianchi, for his valuable comments that helped improve the quality of this paper. ARR is supported by a CFR grant from the AIM laboratory (Saclay, France). This research was, in part, made possible through the financial support of the Agence Nationale de la Recherche (ANR) through the programme SYMPATICO (Program Blanc Projet ANR-11-BS56-0023). IDL is a postdoctoral researcher of the FWO-Vlaanderen (Belgium).

PACS has been developed by MPE (Germany); UVIE (Austria); KU Leuven, CSL, IMEC (Belgium); CEA, LAM (France); MPIA (Germany); INAF-IFSI/OAA/OAP/OAT, LENS, SISSA (Italy); IAC (Spain). This development has been supported by BMVIT (Austria), ESA-PRODEX (Belgium), CEA/CNES (France), DLR (Germany), ASI/INAF (Italy), and CICYT/MCYT (Spain). SPIRE has been developed by Cardiff University (UK); Univ. Lethbridge (Canada); NAOC (China); CEA, LAM (France); IFSI, Univ. Padua (Italy); IAC (Spain); SNSB (Sweden); Imperial College London, RAL, UCL-MSSL, UKATC, Univ. Sussex (UK) and Caltech, JPL, NHSC, Univ. Colorado (USA). This development has been supported by CSA (Canada); NAOC (China); CEA, CNES, CNRS (France); ASI (Italy); MCINN (Spain); Stockholm Observatory (Sweden); STFC (UK); and NASA (USA).

SPIRE has been developed by a consortium of institutes led by Cardiff Univ. (UK) and including: Univ. Lethbridge (Canada); NAOC (China); CEA, LAM (France); IFSI, Univ. Padua (Italy); IAC (Spain); Stockholm Observatory (Sweden); Imperial College London, RAL, UCL-MSSL, UKATC, Univ. Sussex (UK); and Caltech, JPL, NHSC, Univ. Colorado (USA). This development has been supported by national funding agencies: CSA (Canada); NAOC (China); CEA, CNES, CNRS (France); ASI (Italy); MCINN (Spain); SNSB (Sweden); STFC, UKSA (UK); and NASA (USA).

References

Aloisi, A., Clementini, G., Tosi, M., et al. 2007, ApJ, 667, L151
Aloisi, A., van der Marel, R. P., Mack, J., et al. 2005, ApJ, 631, L45
Amblard, A., Cooray, A., Serra, P., et al. 2010, A&A, 518, L9
Anderson, L. D., Zavagno, A., Rodón, J. A., et al. 2010, A&A, 518, L99
Aniano, G., Draine, B. T., Calzetti, D., et al. 2012, ApJ, 756, 138
Asplund, M., Grevesse, N., Sauval, A. J., & Scott, P. 2009, ARA&A, 47, 481
Auld, R., Bianchi, S., Smith, M. W. L., et al. 2013, MNRAS, 428, 1880
Bazell, D. & Dwek, E. 1990, ApJ, 360, 142
Bendo, G. J., Dale, D. A., Draine, B. T., et al. 2006, ApJ, 652, 283
Bendo, G. J., Galliano, F., & Madden, S. C. 2012, MNRAS, 423, 197
Bendo, G. J., Joseph, R. D., Wells, M., et al. 2003, AJ, 125, 2361
Bendo, G. J., Wilson, C. D., Pohlen, M., et al. 2010, A&A, 518, L65
Bergvall, N., Zackrisson, E., Andersson, B.-G., et al. 2006, A&A, 448, 513
Bianchi, S. 2013, A&A, 552, A89
Boquien, M., Calzetti, D., Combes, F., et al. 2011, AJ, 142, 111
Bordalo, V., Plana, H., & Telles, E. 2009, ApJ, 696, 1668
Boselli, A., Ciesla, L., Cortese, L., et al. 2012, A&A, 540, A54
Boselli, A., Lequeux, J., & Gavazzi, G. 2002, A&A, 384, 33
Boselli, A., Lequeux, J., & Gavazzi, G. 2004, A&A, 428, 409
Bot, C., Ysard, N., Paradis, D., et al. 2010, A&A, 523, A20+
Cannon, J. M., Dohm-Palmer, R. C., Skillman, E. D., et al. 2003, AJ, 126, 2806
Cantalupo, C. M., Borrill, J. D., Jaffe, A. H., Kisner, T. S., & Stompor, R. 2010, ApJS, 187, 212
Ciesla, L., Boselli, A., Smith, M. W. L., et al. 2012, A&A, 543, A161
Cormier, D., Lebouteiller, V., Madden, S. C., et al. 2012, A&A, 548, A20
Cormier, D., Madden, S., Lebouteiller, V., Galliano, F., & Hony, S. 2011, in IAU Symposium, Vol. 280, IAU Symposium, 137P
Dale, D. A., Aniano, G., Engelbracht, C. W., et al. 2012, ApJ, 745, 95
Dale, D. A., Gil de Paz, A., Gordon, K. D., et al. 2007, ApJ, 655, 863
de Vaucouleurs, G., de Vaucouleurs, A., Corwin, Jr., H. G., et al. 1991, Third Reference Catalogue of Bright Galaxies, ed. de Vaucouleurs, G., de Vaucouleurs, A., Corwin, H. G., Jr., Buta, R. J., Paturel, G., & Fouque, P. (de Vaucouleurs, G.)
Draine, B. T. & Hensley, B. 2012, ApJ, 757, 103
Draine, B. T. & Lazarian, A. 1998, ApJ, 508, 157
Dumke, M., Krause, M., & Wielebinski, R. 2004, A&A, 414, 475
Dunne, L., Gomez, H. L., da Cunha, E., et al. 2011, MNRAS, 417, 1510
Dupac, X., Bernard, J.-P., Boudet, N., et al. 2003, A&A, 404, L11
Engelbracht, C. W., Gordon, K. D., Rieke, G. H., et al. 2005, ApJ, 628, L29
Engelbracht, C. W., Rieke, G. H., Gordon, K. D., et al. 2008, ApJ, 678, 804
Eskew, M., Zaritsky, D., & Meidt, S. 2012, AJ, 143, 139
Ferrara, A. & Dettmar, R.-J. 1994, ApJ, 427, 155
Galametz, M., Kennicutt, R. C., Albrecht, M., et al. 2012, MNRAS, 425, 763
Galametz, M., Madden, S., Galliano, F., et al. 2009, A&A, 508, 645
Galametz, M., Madden, S. C., Galliano, F., et al. 2011, A&A, 532, A56
Galametz, M., Madden, S. C., Galliano, F., et al. 2010, A&A, 518, L55
Galliano, F., Dwek, E., & Chanial, P. 2008, ApJ, 672, 214
Galliano, F., Hony, S., Bernard, J.-P., et al. 2011, A&A, 536, A88
Galliano, F., Madden, S. C., Jones, A. P., Wilson, C. D., & Bernard, J.-P. 2005, A&A, 434, 867
Galliano, F., Madden, S. C., Jones, A. P., et al. 2003, A&A, 407, 159
Gieren, W., Pietrzyński, G., Nalewajko, K., et al. 2006, ApJ, 647, 1056
Griffin, M. J., Abergel, A., Abreu, A., et al. 2010, A&A, 518, L3
Grocholski, A. J., van der Marel, R. P., Aloisi, A., et al. 2012, AJ, 143, 117
Grossi, M., Hunt, L. K., Madden, S., et al. 2010, A&A, 518, L52
Guseva, N. G., Izotov, Y. I., Fricke, K. J., & Henkel, C. 2012, A&A, 541, A115
Guseva, N. G., Izotov, Y. I., Papaderos, P., & Fricke, K. J. 2007, A&A, 464, 885
Guseva, N. G., Izotov, Y. I., & Thuan, T. X. 2000, ApJ, 531, 776
Guseva, N. G., Papaderos, P., Izotov, Y. I., et al. 2003a, A&A, 407, 91
Guseva, N. G., Papaderos, P., Izotov, Y. I., et al. 2003b, A&A, 407, 105
Israel, F. P., Maloney, P. R., Geis, N., et al. 1996, ApJ, 465, 738
Israel, F. P., Wall, W. F., Raban, D., et al. 2010, A&A, 519, A67
Izotov, Y. I., Chaffee, F. H., Foltz, C. B., et al. 1999, ApJ, 527, 757
Izotov, Y. I., Papaderos, P., Guseva, N. G., Fricke, K. J., & Thuan, T. X. 2004, A&A, 421, 539
Izotov, Y. I., Stasińska, G., Meynet, G., Guseva, N. G., & Thuan, T. X. 2006, A&A, 448, 955
Izotov, Y. I. & Thuan, T. X. 1998, ApJ, 500, 188
Izotov, Y. I., Thuan, T. X., & Lipovetsky, V. A. 1994, ApJ, 435, 647
Izotov, Y. I., Thuan, T. X., & Lipovetsky, V. A. 1997, ApJS, 108, 1

Izotov, Y. I., Thuan, T. X., & Stasińska, G. 2007, ApJ, 662, 15
Juvela, M. & Ysard, N. 2012a, A&A, 541, A33
Juvela, M. & Ysard, N. 2012b, A&A, 539, A71
Karachentsev, I. D., Dolphin, A. E., Geisler, D., et al. 2002, A&A, 383, 125
Karachentsev, I. D., Karachentseva, V. E., Huchtmeier, W. K., & Makarov, D. I. 2004, AJ, 127, 2031
Karachentsev, I. D., Sharina, M. E., Dolphin, A. E., et al. 2003, A&A, 398, 467
Kelly, B. C., Shetty, R., Stutz, A. M., et al. 2012, ApJ, 752, 55
Kennicutt, R. C., Calzetti, D., Aniano, G., et al. 2011, PASP, 123, 1347
Kennicutt, Jr., R. C. 1998, ApJ, 498, 541
Kennicutt, Jr., R. C., Armus, L., Bendo, G., et al. 2003, PASP, 115, 928
Kim, M., Kim, E., Hwang, N., et al. 2009, ApJ, 703, 816
Kobulnicky, H. A., Kennicutt, Jr., R. C., & Pizagno, J. L. 1999, ApJ, 514, 544
Kobulnicky, H. A. & Skillman, E. D. 1997, ApJ, 489, 636
Kong, X., Cheng, F. Z., Weiss, A., & Charlot, S. 2002, A&A, 396, 503
Lebouteiller, V., Cormier, D., Madden, S. C., et al. 2012, A&A, 548, A91
Lee, H. & Skillman, E. D. 2004, ApJ, 614, 698
Lee, H., Skillman, E. D., & Venn, K. A. 2006, ApJ, 642, 813
Lequeux, J., Peimbert, M., Rayo, J. F., Serrano, A., & Torres-Peimbert, S. 1979, A&A, 80, 155
Leroy, A. K., Bolatto, A., Gordon, K., et al. 2011, ApJ, 737, 12
Leroy, A. K., Walter, F., Bigiel, F., et al. 2009, AJ, 137, 4670
López-Sánchez, Á. R., Esteban, C., & Rodríguez, M. 2004, ApJS, 153, 243
Lynds, R., Tolstoy, E., O'Neil, Jr., E. J., & Hunter, D. A. 1998, AJ, 116, 146
Madden, S. C. 2000, New A Rev., 44, 249
Madden, S. C., Galliano, F., Jones, A. P., & Sauvage, M. 2006, A&A, 446, 877
Madden, S. C., Poglitsch, A., Geis, N., Stacey, G. J., & Townes, C. H. 1997, ApJ, 483, 200
Madden, S. C., Rémy, A., Galliano, F., et al. 2012, in IAU Symposium, Vol. 284, IAU Symposium, ed. R. J. Tuffs & C. C. Popescu, 141–148
Madden, S. C., Rémy-Ruyer, A., Galametz, M., et al. 2013, PASP, 125, 600
Magrini, L. & Gonçalves, D. R. 2009, MNRAS, 398, 280
Masegosa, J., Moles, M., & Campos-Aguilar, A. 1994, ApJ, 420, 576
McCall, M. L., Rybski, P. M., & Shields, G. A. 1985, ApJS, 57, 1
Meny, C., Gromov, V., Boudet, N., et al. 2007, A&A, 468, 171
Moles, M., Marquez, I., Masegosa, J., et al. 1994, ApJ, 432, 135
Moll, S. L., Mengel, S., de Grijs, R., Smith, L. J., & Crowther, P. A. 2007, MNRAS, 382, 1877
Mould, J. R., Huchra, J. P., Freedman, W. L., et al. 2000, ApJ, 529, 786
Murphy, E. J., Helou, G., Condon, J. J., et al. 2010, ApJ, 709, L108
O'Halloran, B., Satyapal, S., & Dudik, R. P. 2006, ApJ, 641, 795
Ott, S. 2010, in Astronomical Society of the Pacific Conference Series, Vol. 434, Astronomical Data Analysis Software and Systems XIX, ed. Y. Mizumoto, K.-I. Morita, & M. Ohishi, 139
Papadopoulos, P. P., Thi, W.-F., & Viti, S. 2004, MNRAS, 351, 147
Paradis, D., Bernard, J.-P., & Mény, C. 2009, A&A, 506, 745
Paradis, D., Veneziani, M., Noriega-Crespo, A., et al. 2010, A&A, 520, L8
Pilbratt, G. L., Riedinger, J. R., Passvogel, T., et al. 2010, A&A, 518, L1
Pilyugin, L. S. & Thuan, T. X. 2005, ApJ, 631, 231
Planck Collaboration, Ade, P. A. R., Aghanim, N., et al. 2011a, A&A, 536, A19
Planck Collaboration, Ade, P. A. R., Aghanim, N., et al. 2011b, A&A, 536, A20
Poglitsch, A., Krabbe, A., Madden, S. C., et al. 1995, ApJ, 454, 293
Poglitsch, A., Waelkens, C., Geis, N., et al. 2010, A&A, 518, L2
Popescu, C. C. & Hopp, U. 2000, A&AS, 142, 247
Pustilnik, S. A., Kniazev, A. Y., Pramskij, A. G., Ugryumov, A. V., & Masegosa, J. 2003, A&A, 409, 917
Reach, W. T., Dwek, E., Fixsen, D. J., et al. 1995, ApJ, 451, 188
Roussel, H. 2012, ArXiv:1205.2576
Sauvage, M., Vigroux, L., & Thuan, T. X. 1990, A&A, 237, 296
Saviane, I., Ivanov, V. D., Held, E. V., et al. 2008, A&A, 487, 901
Schruba, A., Leroy, A. K., Walter, F., et al. 2012, AJ, 143, 138
Schulte-Ladbeck, R. E., Hopp, U., Greggio, L., Crone, M. M., & Drozdovsky, I. O. 2001, AJ, 121, 3007
Sharina, M. E., Karachentsev, I. D., & Tikhonov, N. A. 1996, A&AS, 119, 499
Shetty, R., Kauffmann, J., Schnee, S., & Goodman, A. A. 2009a, ApJ, 696, 676
Shetty, R., Kauffmann, J., Schnee, S., Goodman, A. A., & Ercolano, B. 2009b, ApJ, 696, 2234
Skibba, R. A., Engelbracht, C. W., Dale, D., et al. 2011, ApJ, 738, 89
Skillman, E. D., Côté, S., & Miller, B. W. 2003, AJ, 125, 610
Smith, M. W. L., Eales, S. A., Gomez, H. L., et al. 2012a, ApJ, 756, 40
Smith, M. W. L., Gomez, H. L., Eales, S. A., et al. 2012b, ApJ, 748, 123
Stepnik, B., Abergel, A., Bernard, J.-P., et al. 2001, in Astronomical Society of the Pacific Conference Series, Vol. 243, From Darkness to Light: Origin and Evolution of Young Stellar Clusters, ed. T. Montmerle & P. André, 47
Thuan, T. X., Izotov, Y. I., & Lipovetsky, V. A. 1995, ApJ, 445, 108
Tosi, M., Sabbi, E., Bellazzini, M., et al. 2001, AJ, 122, 1271
Tully, R. B. 1988, Nearby galaxies catalog (Cambridge University Press)
Ugryumov, A. V., Engels, D., Pustilnik, S. A., et al. 2003, A&A, 397, 463
van Zee, L. & Haynes, M. P. 2006, ApJ, 636, 214
van Zee, L., Haynes, M. P., Salzer, J. J., & Broeils, A. H. 1996, AJ, 112, 129
Walter, F., Cannon, J. M., Roussel, H., et al. 2007, ApJ, 661, 102
Wilson, C. D. 1995, ApJ, 448, L97
Wilson, C. D. 2005, in IAU Symposium, Vol. 231, Astrochemistry: Recent Successes and Current Challenges, ed. D. C. Lis, G. A. Blake, & E. Herbst, 271–280
Yang, M. & Phillips, T. 2007, ApJ, 662, 284
Ysard, N., Juvela, M., Demyk, K., et al. 2012, A&A, 542, A21
Ysard, N. & Verstraete, L. 2010, A&A, 509, A12
Zhu, M., Papadopoulos, P. P., Xilouris, E. M., Kuno, N., & Lisenfeld, U. 2009, ApJ, 706, 941
Zibetti, S., Charlot, S., & Rix, H.-W. 2009, MNRAS, 400, 1181
Zubko, V., Dwek, E., & Arendt, R. G. 2004, ApJS, 152, 211

Appendix A: Modified blackbody fits for the Dwarf Galaxy Survey

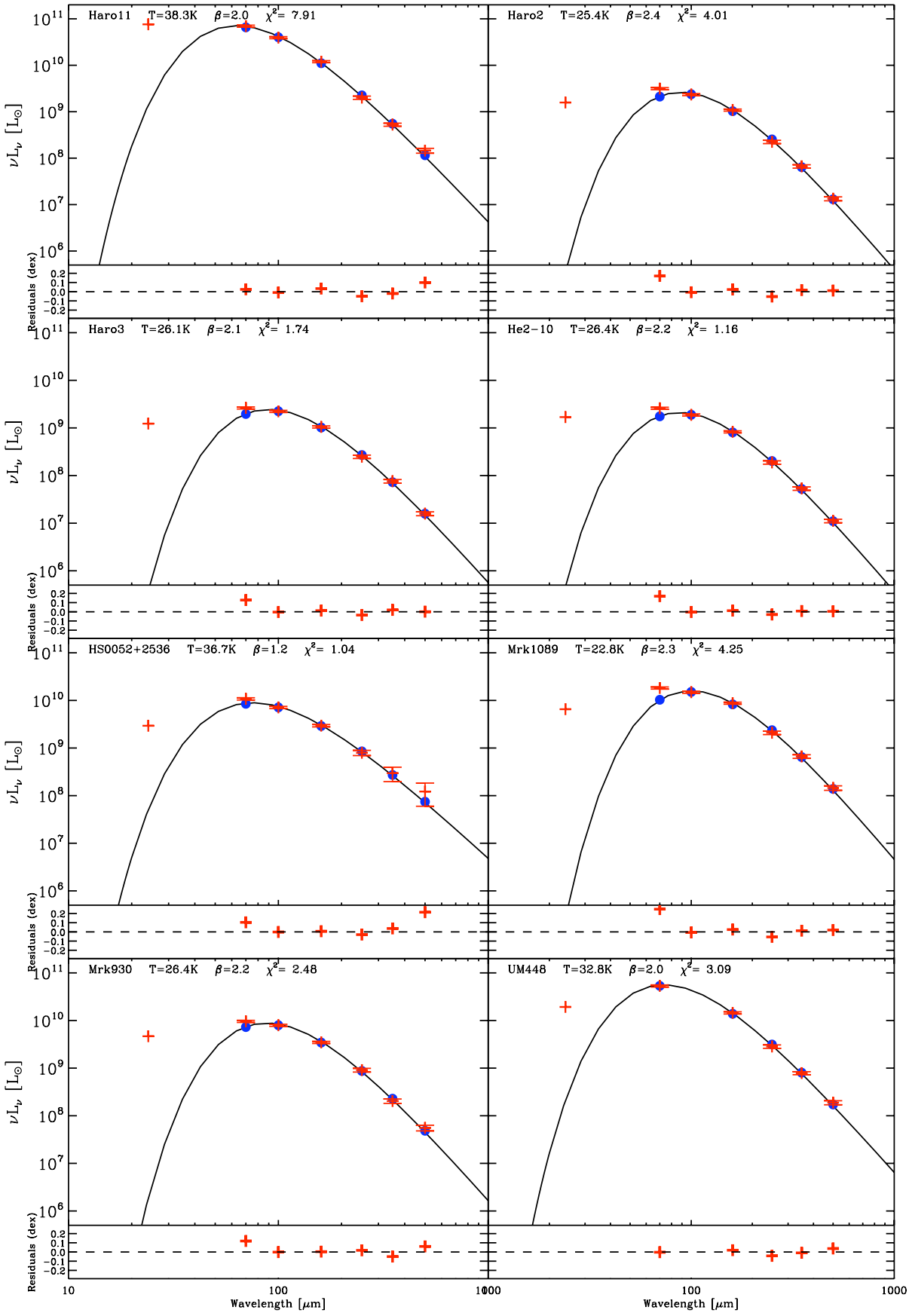

Fig. A.1. Modified blackbody fits of the 70 to 500 μm range for the DGS. The solid black line is the modelled modified blackbody, the blue circles are the modelled points. The red symbols are the observations: crosses are for detections and diamonds are for upper limits. We overlay the MIPS 24 μm point from Bendo et al. (2012). The T and β parameters are indicated on the top of each plot along with the χ^2 value of the fit. The bottom panel of each plot indicates the residuals from the fit.

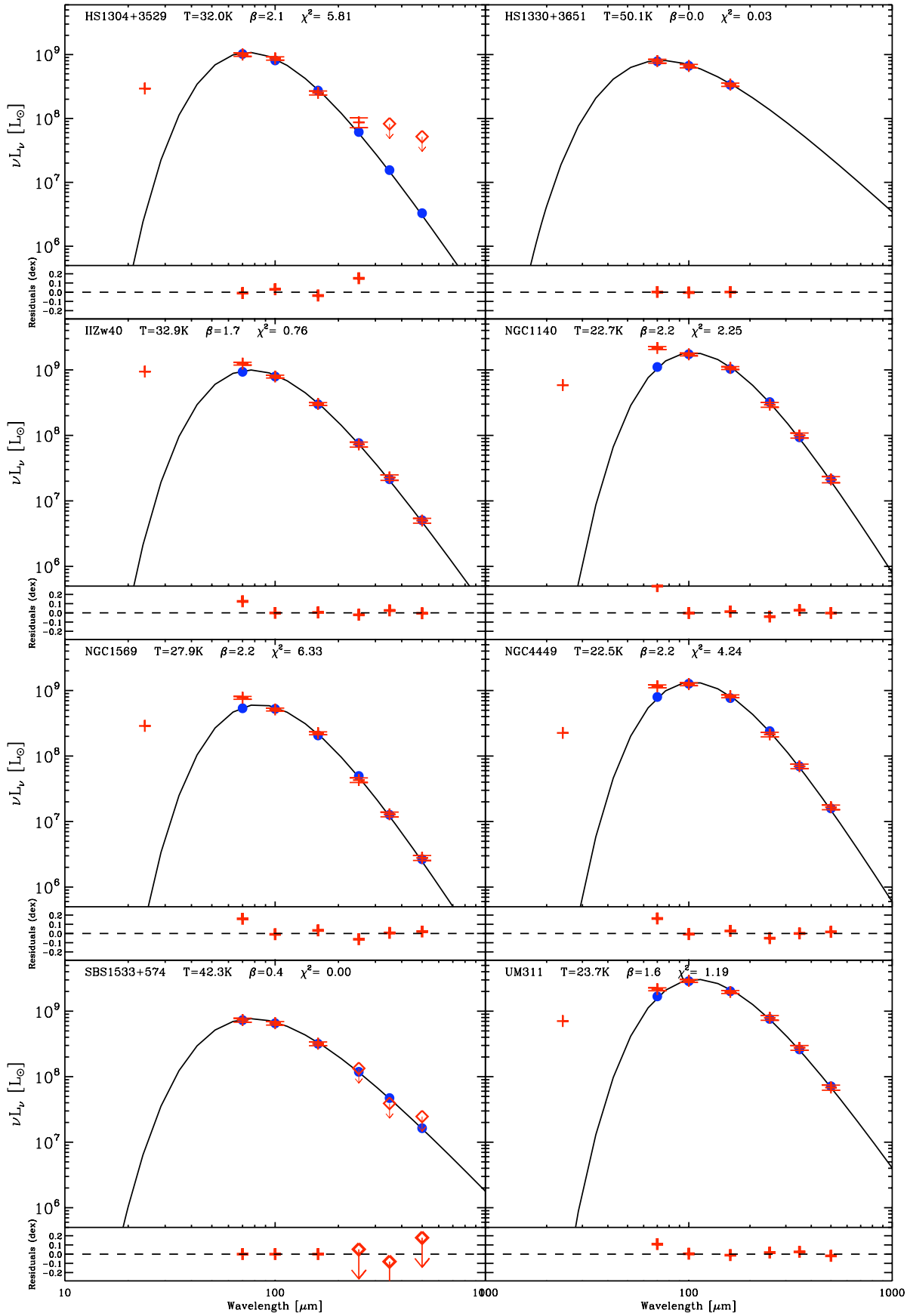

Fig. A.1. *(continued)* Modified blackbody fits of the 70 to 500 μm range for the DGS.

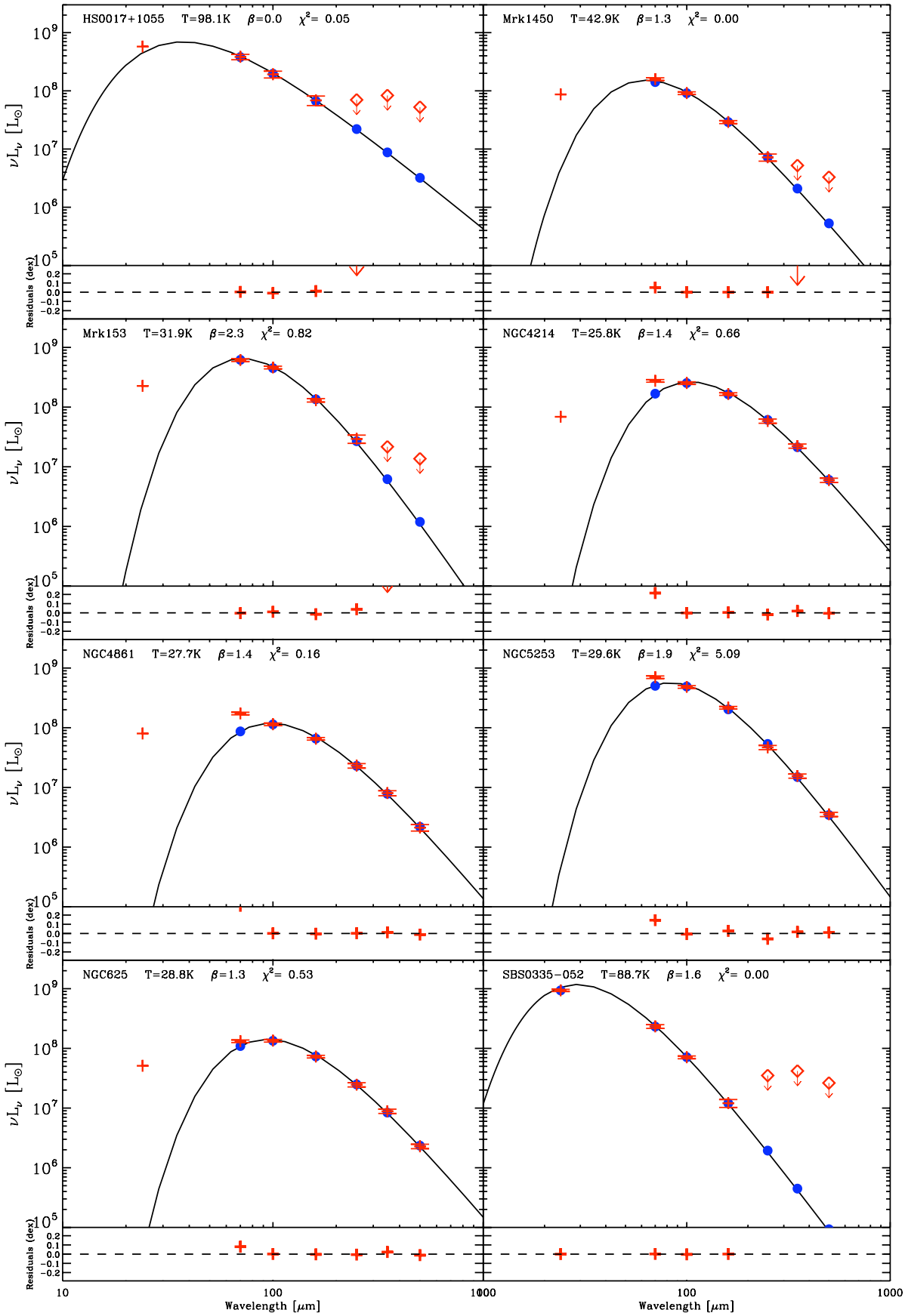

Fig. A.1. *(continued)* Modified blackbody fits of the 70 to 500 μm range for the DGS. Note: for SBS0335-052, we included the 24 μm point in the fit as the 24 μm point fell below the modelled modified blackbody when we just overlaid it on the plot.

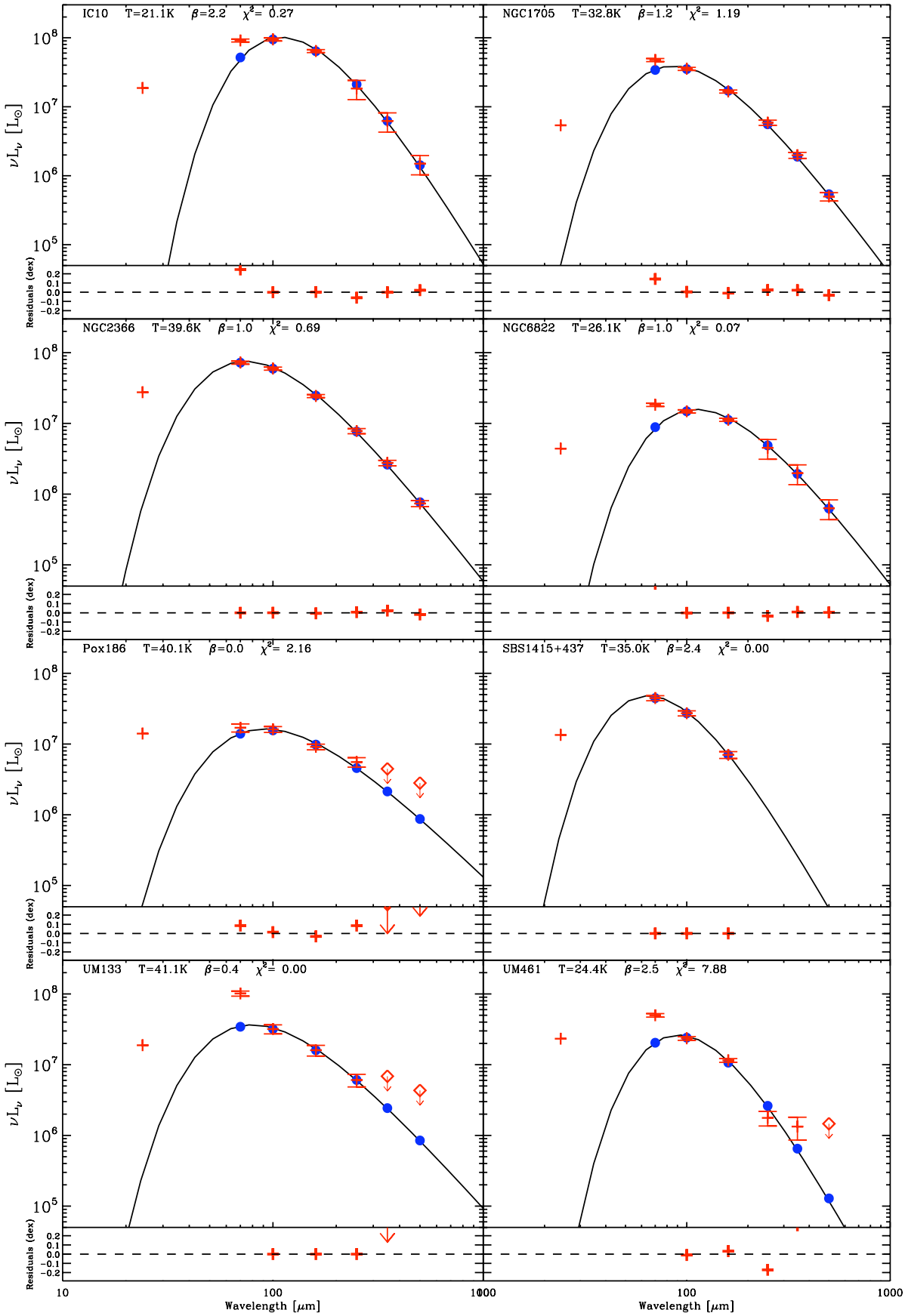

Fig. A.1. *(continued)* Modified blackbody fits of the 70 to 500 μm range for the DGS.

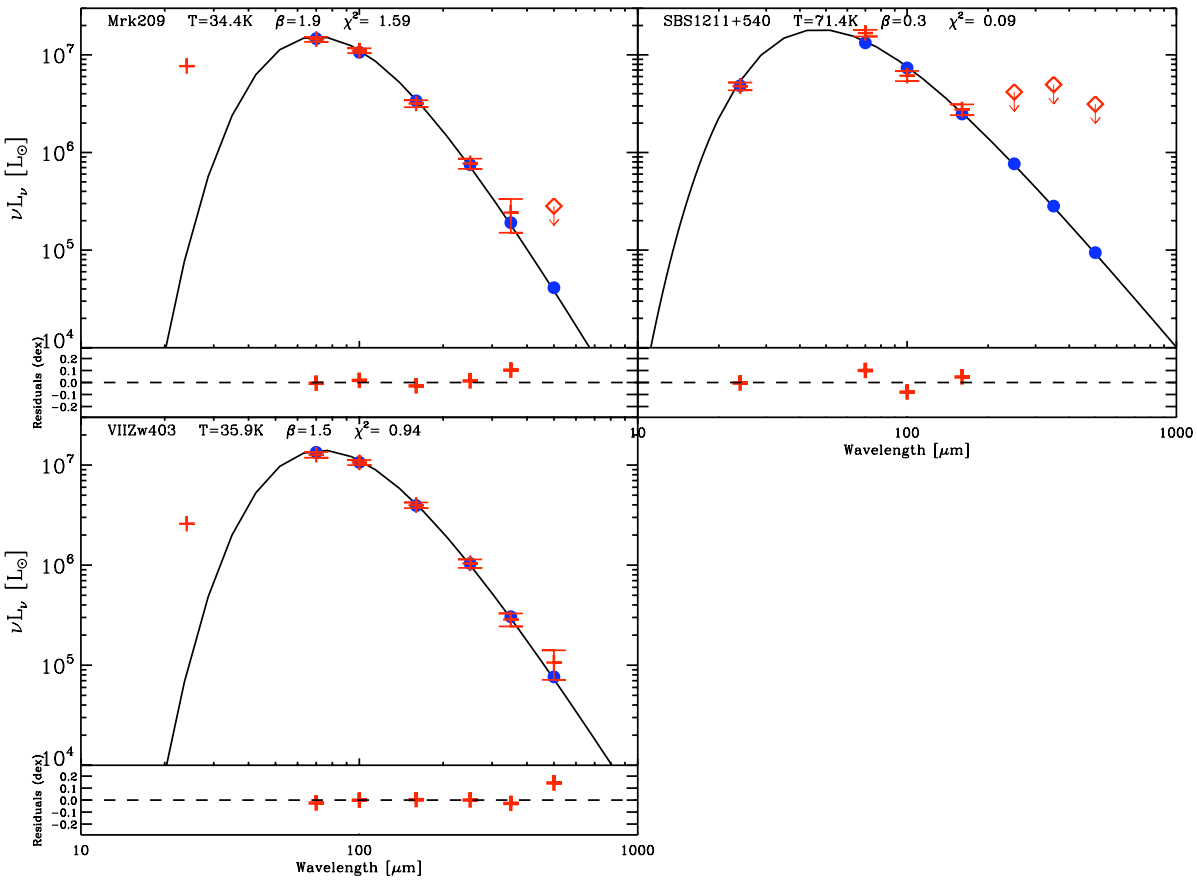

Fig. A.1. *(continued)* Modified blackbody fits of the 70 to 500 μm range for the DGS. Note: for SBS1211+540, we included the 24 μm point in the fit as the 24 μm point fell below the modelled modified blackbody when we just overlaid it on the plot.